J. Fluid Mech. (2024), *vol*. 993, A4, doi:10.1017/jfm.2024.558

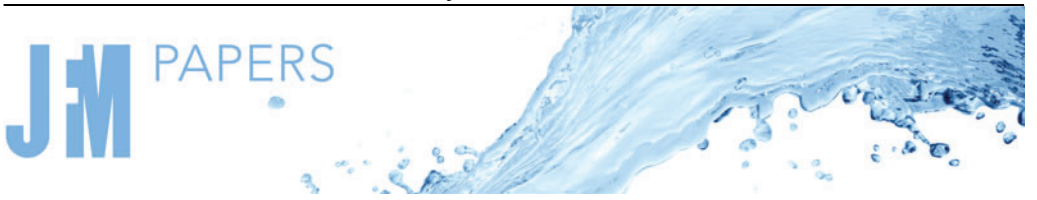

A combined active control method of restricted nonlinear model and machine learning technology for drag reduction in turbulent channel flow

Bing-Zheng Han[1], **Wei-Xi Huang**[1],† **and Chun-Xiao Xu** [1]

[1]AML, Department of Engineering Mechanics, Tsinghua University, Beijing 100084, PR China

(Received 20 January 2024; revised 13 July 2024; accepted 15 July 2024)

The practical implementation of machine learning in flow control is limited due to its significant training expenses. In the present study the convolutional neural network (CNN) trained with the data of the restricted nonlinear (RNL) model is used to predict the normal velocity on a detection plane at $y^+ = 10$ in a turbulent channel flow, and the predicted velocity is used as wall blowing and suction for drag reduction. An active control test is carried out by using the well-trained CNN in direct numerical simulation (DNS). Substantial drag reduction rates up to 19 % and 16 % are obtained based on the spanwise and streamwise wall shear stresses, respectively. Furthermore, we explore the online control of wall turbulence by combining the RNL model with reinforcement learning (RL). The RL is constructed to determine the optimal wall blowing and suction based on its observation of the wall shear stresses without using the label data on the detection plane for training. The controlling and training processes are conducted synchronously in a RNL flow field. The control strategy discovered by RL has similar drag reduction rates with those obtained previously by the established method. Also, the training cost decreases by over thirty times at $Re_\tau = 950$ compared with the DNS-RL model. The present results provide a perspective that combining the RNL model with machine learning control for drag reduction in wall turbulence can be effective and computationally economical. Also, this approach can be easily extended to flows at higher Reynolds numbers.

Key words: drag reduction, turbulence control, machine learning

† Email address for correspondence: hwx@tsinghua.edu.cn

1. Introduction

Flow control for drag reduction in the wall turbulence is of vital importance in industrial applications. Researchers have pointed out that the production of high friction drag in turbulence is closely related to the coherent structures near the wall (Kravchenko, Choi & Moin 1993). Hamilton, Kim & Waleffe (1995) revealed that the regeneration process of near-wall coherent structures included three phases: the formation of streaks by streamwise vortices, the breakdown of streaks and the regeneration of streamwise vortices, based on direct numerical simulation (DNS) of the plane Couette turbulent flow. A common characteristic of the effective control methods for drag reduction is the attenuation of the near-wall streamwise vortices (Kim 2011). Choi, Moin & Kim (1994) initially introduced an active control scheme, known as the opposition control. It involves applying wall blowing and suction, whose normal velocity is opposite to that observed on a near-wall detection plane to offset the sweep and ejection motions caused by the streamwise vortices. The aim is to weaken the Reynolds shear stress, suppress turbulence and reduce the wall friction drag. Several studies have tried to explain the mechanism underlying drag reduction by opposition control. Hammond, Bewley & Moin (1998) and Chung & Talha (2011) pointed out that a 'virtual wall' with approximately nothrough flow was formed halfway between the wall and the detection plane because of the wall blowing and suction. Furthermore, Deng & Xu (2012) illustrated that opposition control can suppress the production of streamwise vorticity by weakening the near-wall normal velocity, from the point of view of the transient growth mechanism (Schoppa & Hussain 2002). The influence of some parameters on the control effect has been investigated in a number of studies. It was reported that the drag reduction rate is decreased with the Reynolds number. For example, approximately 26 % drag reduction was obtained at $Re_\tau = 100$, whereas it was reduced to 19 % at $Re_\tau = 720$ (Chang, Collis & Ramakrishnan 2002) and 18 % at $Re_\tau = 1000$ (Deng, Huang & Xu 2016), where $Re_\tau = u_\tau \delta/\mu$, u_τ is the wall shear velocity, δ is the channel half-height and μ is the kinematic viscosity. Deng *et al.* (2016) pointed out that the origin of effectiveness degradation lay in the modulation of the amplitudes of near-wall coherent structures by large-scale motions in higher Reynolds numbers. Chang *et al.* (2002) and Deng *et al.* (2016) also showed that there exists an optimal height that is decreased with the Reynolds number, i.e. $y^+ \approx 15$ at $Re_\tau = 180$, $y^+ \approx 14$ at $Re_\tau = 590$ and $y^+ \approx 13$ at $Re_\tau = 1000$, where $y^+ = yu_\tau/\mu$, y is the normal distance from the wall. Furthermore, Chung & Talha (2011) found that the drag was reduced by 16 % with the detection plane at $y^+ = 20$ but increased by 17 % with the detection plane at $y^+ = 23$. Deng & Xu (2012) showed that the $y^+ < 20$ and $y^+ > 20$ controls were, respectively, anti-phase and in-phase manipulations to the near-wall vertical velocity. By changing the amplitude of the wall blowing and suction, they proposed the strengthened in-phase control and the weakened anti-phase control to improve the efficiency of opposition control, and obtained drag reduction successfully for different detection plane locations.

In recent decades, methods of determining the optimal distribution of normal velocities used for wall blowing and suction based on measurable physical quantities at the wall have been invented. This is to prevent the difficulty of placing sensors inside the flow field in real practice when the opposition control is applied. Based on the Taylor series expansion of the normal velocity near the wall, Choi *et al.* (1994) indicated a high correlation coefficient of about 0.75 between the wall-normal velocities (v) at $y^+ = 10$ and $(\partial/\partial z)/\partial w/\partial y|_w$ at the wall through their joint probability density. But, a v control based on $(\partial/\partial z)/\partial w/\partial y|_w$ yielded only about 6 % reduction of drag. A variational adjoint-based state estimation algorithm proposed by Bewley & Protas (2004) improved the prediction performance to 0.88 based on three kinds of quantities: wall pressure, streamwise and spanwise wall

shear stresses. It resulted in a better correlation between them and v at $y^+ = 10$. Using the spanwise wall shear stress or wall pressure as input, a suboptimal control method proposed by Lee, Kim & Choi (1998) successfully obtained effective wall blowing and suction similar to that of the opposition control with a drag reduction rate of up to 22 %. However, their attempt based on the streamwise wall shear stress failed to reduce drag because of the oversimplified state equation used in the suboptimal procedure (Kasagi, Suzuki & Fukagata 2009). Feedback control proposed by Koumoutsakos (1999), in which the manipulation of the vorticity flux components is employed based on the information of wall pressure, showed similar control efficiency to or better than the opposition control. Lee *et al.* (2001) designed a linear quadratic-Gaussian/loop-transfer-recovery controller. It reduced the skin friction by 10 % at the friction Reynolds number $Re_\tau = 100$ using the streamwise wall shear stress. Also, Morimoto *et al.* (2002) developed and optimized a control scheme with the aid of genetic algorithms based on the streamwise wall shear stress. They obtained a 12 % drag reduction rate. Fukagata & Kasagi (2004) further improved the suboptimal control of Lee *et al.* (1998) by using the near-wall Reynolds shear stress as the cost function. They obtained a drag reduction rate of up to 11.5 % in turbulent channel flow at $Re_\tau = 180$ by using the streamwise wall shear stress.

Recently, with the development of machine learning, there have been various applications to active flow control problems. For drag reduction in wall turbulence, a pioneering work by Lee *et al.* (1997) utilized a neural network to represent the relationship between the spanwise wall shear stress and the normal velocity at $y^+ = 10$. Applying the normal velocity predicted by the neural network for wall blowing and suction, they obtained a drag reduction of 20 %, which was close to that of the opposition control. Although with different methods, the control strategy with the input of spanwise wall shear stress was verified once again using the suboptimal control (Lee *et al.* 1998). This indicates that the trained neural network acts as an effective predictor of v at $y^+ = 10$ using spanwise wall shear stress. Lorang, Podvin & Le Quéré (2008) applied a similar multi-layer neural network method in Fourier space to identify the optimal velocity length scales associated with substantial drag reduction. But both of them pointed out that using streamwise wall shear stress did not improve or even reduce the efficiency of neural network-based control. It is noticed that convolutional neural network (CNN) has been widely applied in fluid mechanics because of its strong feature-extraction capability especially for two-dimensional figures. Examples include super-resolution reconstruction (Fukami *et al.* 2019), prediction of the flow field information (Guo, Li & Iorio 2016; Kim & Lee 2020) and so on. Han & Huang (2020) developed an active controller based on CNN to predict v at $y^+ = 10$ used for wall blowing and suction based on spanwise or streamwise wall shear stress at $Re_\tau = 100, 180, 390$. It was found that for spanwise wall shear stress, a linear single-layer CNN similar to that of Lee *et al.* (1997) was enough to realize good prediction and substantial drag reduction; while for streamwise wall shear stress, a multiple nonlinear CNN architecture was necessary. Based on the constructed CNN control models, we obtained up to 19 % and 15 % drag reduction based on the spanwise and streamwise wall shear stresses, respectively. Park & Choi (2020) designed a larger CNN architecture using wall pressure, streamwise or spanwise wall shear stress as input in order to extend the CNN model trained by the data from lower-Reynolds-number flow to control the flow at a higher Reynolds number. They trained the CNN model at $Re_\tau = 180$ and obtained up to 17 %, 11 % and 18 % drag reduction at $Re_\tau = 180$ and 11 %, 6 % and 15 % drag reduction at $Re_\tau = 578$, based on wall pressure, streamwise and spanwise wall shear stresses, respectively.

On the other hand, a semi-supervised machine learning method of reinforcement learning (RL) has also been applied to flow control problems (Rabault *et al.* 2019; Fan

et al. 2020*a*; Tang *et al.* 2020; Han, Huang & Xu 2022). Especially, Sonoda *et al.* (2023) and Lee, Kim & Lee (2023) firstly introduced RL to the turbulent channel flow for drag reduction. Sonoda *et al.* (2023) used velocities at the detection plane as input of RL and optimized a constant multiplication coefficient. Then, the normal velocity multiplied by that constant was used as wall blowing and suction. This method was based on the strengthened opposition controller (Chung & Talha 2011), whose strength was chosen intelligently by RL, and a larger drag reduction rate was obtained than that of the traditional opposition control. In Lee *et al.* (2023) the control model used the wall shear stress as the input of RL and directly outputted the wall blowing and suction, where RL was trained to obtain a larger drag reduction rate by adjusting its output. This RL control model removes the limitation of the label data on the detection plane and allows for exploring a better control strategy than that of the opposition control. Unlike the supervised learning (SL) control model based on CNN with an offline learning process, the training of the RL model and control of the flow field are carried out simultaneously, which is known as the online training. In general, it is challenging to apply the RL to flow control, because its training process is always accompanied by a large number of simulations of the controlled flow field, resulting in an extremely high computational cost. Thus, the RL control models are all restrained within the flow field at low Reynolds numbers. It is a consensus that the cost of the numerical simulation of flow field is much larger than that of RL. For example, the simulation accounts for approximately 89 % of the total computation cost of RL control (Lee *et al.* 2023), suggesting that accelerating the flow simulation will greatly reduce the cost of training an RL control model. In the current work we attempt to couple the physical reduced-order model with machine learning to control the turbulent channel flow for drag reduction. The aim is to extend the application of the machine learning control model to wall turbulence at higher Reynolds numbers.

The restricted nonlinear (RNL) model system divides the flow into streamwise streaks, vortices and fluctuations (Alizard & Biau 2019). It simplifies the Navier–Stokes (N-S) equations by parametrizing or neglecting the nonlinear interactions among the varying perturbations while retaining the interaction between them and the streamwise constant mean flow (Thomas *et al.* 2014). Farrell & Ioannou (2012) applied the RNL model to Couette flows by parametrizing the perturbation–perturbation interactions as an additive stochastic forcing. They found that it could support a realistic self-sustaining process after the flow transitions even though the forcing was removed. Thomas *et al.* (2014, 2015) investigated the dynamics of RNL turbulence systematically to examine the implications of its simplified structure for the wall turbulence of plane Couette flow. They revealed that a small number of streamwise varying modes or even as few as one mode can suffice to sustain the turbulent state, which can be used as a physics-based approach to simplify the flow representation (Gayme & Minnick 2019). The RNL turbulence at moderate Reynolds numbers of $Re_\tau = 180$–340 in half-channel flow was investigated by Bretheim, Meneveau & Gayme (2015). The results showed that a band-limited RNL system using one or a few determined modes improved its prediction of the mean velocity profile and second-order statistics. Farrell *et al.* (2016) further studied the RNL turbulence of channel flow at $Re_\tau = 950$ and illustrated that the roll/streak dynamics supporting the turbulence in the buffer and logarithmic layers in the RNL model were essentially similar to that in DNS. Their results also pointed out that because the RNL and DNS turbulences were sustainable with almost the same pressure gradient, the sum of Reynolds stresses was the same linear function of the height away from the wall and the RNL model produced Reynolds stresses very similarly with those in DNS. Compared with other reduced-order models, e.g. proper orthogonal decomposition (Smith, Moehlis & Holmes 2005) and the minimal flow unit

(Jiménez & Moin 1991), the RNL model is computationally economic with its simplified dynamical setting requiring fewer streamwise modes for self-sustaining turbulence. Also, it does not rely on the Reynolds number or channel size since it is directly derived from the N-S equations.

In the present study the RNL model is coupled with machine learning to control a fully developed turbulent channel flow for drag reduction. A CNN is constructed to determine the optimal wall blowing and suction with the input of wall shear stresses. Based on the opposition control put forward by Choi *et al.* (1994), SL is utilized to train the CNN based on the error between its output and the normal velocity at $y^+ = 10$, which is represented as the RNL-SL control model. The RNL-SL control model is trained by utilizing the data from the RNL flow field, which exhibits flow characteristics that are comparable to those observed in DNS. However, it is restricted in the streamwise direction to the benefit of decreasing the complexity and cost of training. The prediction performance of the RNL-SL model trained by RNL data is compared on RNL and DNS flow fields. Then, it is applied to the DNS flow for active control. Furthermore, exploration of the RL control method coupled with the RNL model is introduced. The RL trains the CNN through the reward obtained from its online control of the RNL field, which is represented as the RNL-RL control model. Both the training process and control effects are compared with those of RNL-SL. Numerical tests are carried out in the flows at three different Reynolds numbers of $Re_\tau = 100, 180, 950$ to verify the capacity of the combined method of RNL and machine learning. In the following, details of the RNL simulation, frameworks of RNL-SL and RNL-RL control models are presented in § 2. The training process, prediction performance and active control results of the RNL-SL model are shown in § 3. The training process and control strategy of the RNL-RL model are given in § 4, followed by conclusions in § 5.

2. Methodology

2.1. *The RNL model*

The base flow is a fully developed turbulent channel flow, of which the streamwise, wall-normal and spanwise directions are denoted by x, y and z, respectively. Since the turbulent channel flow is uniform along the streamwise direction in the RNL model, the velocity and pressure fields $\boldsymbol{u}(x, y, z, t), p(x, y, z, t)$ are decomposed into the streamwise averaged $\boldsymbol{U}(y, z, t)$, $P(y, z, t)$ and the perturbations $\boldsymbol{u}'(x, y, z, t)$, $p'(x, y, z, t)$ from them, respectively (Farrell *et al.* 2016). The corresponding governing equations, derived from the incompressible N–S and continuity equations, can be expressed as

$$\boldsymbol{U}_t + \boldsymbol{U}\cdot\nabla\boldsymbol{U} + \nabla P - \nu\nabla^2\boldsymbol{U} = -\langle\boldsymbol{u}'\cdot\nabla\boldsymbol{u}'\rangle_x, \tag{2.1}$$

$$\boldsymbol{u}'_t + \boldsymbol{U}\cdot\nabla\boldsymbol{u}' + \boldsymbol{u}'\cdot\nabla\boldsymbol{U} + \nabla p' - \nu\nabla^2\boldsymbol{u}' = 0, \tag{2.2}$$

$$\nabla\cdot\boldsymbol{U} = 0, \nabla\cdot\boldsymbol{u}' = 0, \tag{2.3}$$

where ν is the kinematic viscosity and the quantities are non-dimensionalized by the channel half-width δ and the mean velocity U_m. The difference between RNL and N-S equations is due to the approximation of the RNL model, in which the perturbation–perturbation interaction term $-\boldsymbol{u}'\cdot\nabla\boldsymbol{u}' + \langle\boldsymbol{u}'\cdot\nabla\boldsymbol{u}'\rangle_x$ is set to zero in the present study. The RNL system remains the interaction of the perturbations on the streamwise mean flow field, $\boldsymbol{U}$, which acts as a driven term of (2.1), i.e. the divergence of the streamwise mean Reynolds stress. Reynolds stresses are solved by (2.2), which describes the dynamics of the perturbation flow, $\boldsymbol{u}'$, under the influence of $\boldsymbol{U}$. Previous

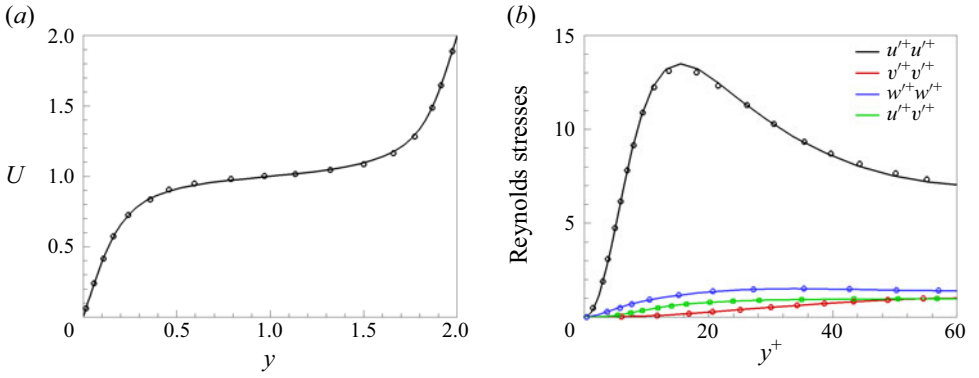

Figure 1. Comparison of the mean velocity profile and Reynolds stresses of a plane Couette flow solved by the RNL model between the present results (lines) and those from Thomas *et al.* (2014) (circular symbols).

Cases	Re_τ	$L_x \times L_y \times L_z$	$N_x \times N_y \times N_z$	CPU time for single computational time step
RNL100	95.98	$4\pi \times 2 \times 4\pi/3$	$10 \times 64 \times 32$	0.008
DNS100	99.32	$4\pi \times 2 \times 4\pi/3$	$32 \times 64 \times 32$	0.020
RNL180	170.10	$2\pi \times 2 \times \pi$	$16 \times 128 \times 128$	0.037
DNS180	178.25	$2\pi \times 2 \times \pi$	$128 \times 128 \times 128$	0.205
RNL950	838.08	$2\pi \times 2 \times \pi$	$16 \times 384 \times 512$	0.425
DNS950	930.56	$2\pi \times 2 \times \pi$	$512 \times 384 \times 512$	13.268

Table 1. Computational parameters for the RNL model and DNS of turbulent channel flow.

studies (Constantinou *et al.* 2014; Bretheim *et al.* 2015; Farrell *et al.* 2016) have revealed that these essential nonlinear interactions are necessary for a self-sustained turbulent state, and dynamical restriction makes RNL simulation more computationally efficient.

The RNL equations are solved based on the second-order central finite-difference discretization on a staggered grid and are advanced with the Crank–Nicholson scheme in time. The fractional step method is adopted for velocity–pressure decoupling (Kim, Baek & Sung 2002). To verify the numerical accuracy of the RNL solver, a plane Couette flow at a Reynolds number of $Re = 1000$ is simulated. The computational domains and number of grid points in the x, y, z directions are $L_x = 4\pi, L_y = 2, L_z = 4\pi$ and $N_x = 16, N_y = 64, N_z = 128$, respectively, which are the same with those of Thomas *et al.* (2014). The friction Reynolds numbers Re_τ of DNS and the RNL model are 66.14 and 64.91, respectively, close to those of Thomas *et al.* (2014), i.e. 66.2 and 64.9. Also, we compare the turbulent mean velocity profile and time-averaged Reynolds stresses obtained from the RNL simulation in figure 1. The results agree very well with the reference data, validating the computational accuracy of our RNL solver.

In this paper we aim to replace the DNS of turbulent channel flow with the RNL model to accelerate the numerical simulation to obtain the basic characteristic of the flow field and the prediction of the drag. Based on that, we limit the number of grids in the streamwise direction (N_x) to a few and let N_y, N_z be the same as those of DNS, as shown in table 1.

The friction Reynolds number of the RNL model is almost equal to that of DNS, but the difference between them increases with Reynolds number. Figure 2 shows that RNL system overpredicts the mean streamwise velocity for $y^+ > 10$ and the slope and intercept

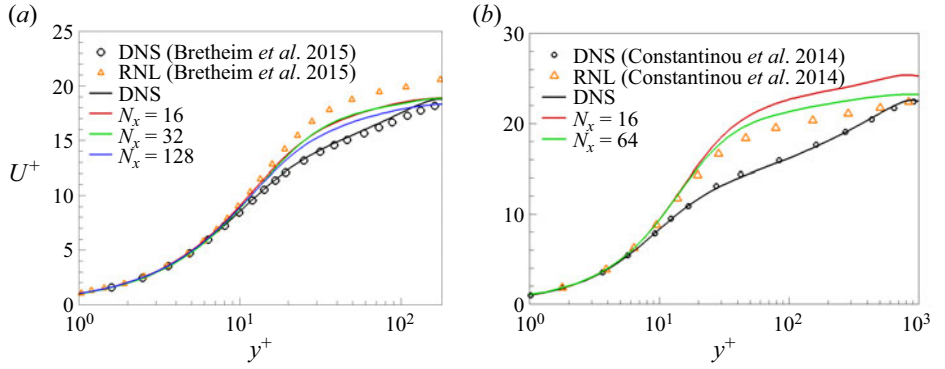

Figure 2. Mean streamwise velocity profiles from the RNL model with different streamwise grid numbers compared with that from DNS: (*a*) $Re_\tau = 180$, (*b*) $Re_\tau = 950$.

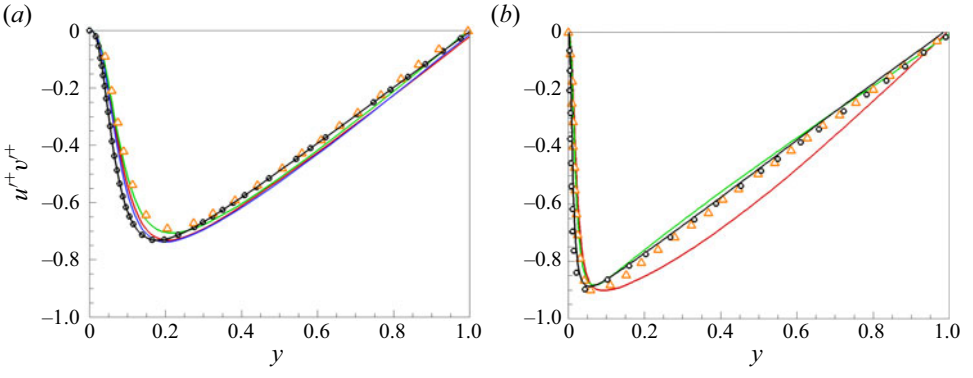

Figure 3. Comparison of the Reynolds stress components, $u'^+v'^+$, in the same cases shown in figure 2.

of the logarithmic region are not consistent with DNS, which also appear in the baseline RNL cases without any mode limiting of Bretheim *et al.* (2015) in a half-channel at $Re_\tau = 180$ and the case of Constantinou *et al.* (2014) at $Re_\tau = 950$. Bretheim *et al.* (2015) and Gayme & Minnick (2019) also detected that restricting the streamwise wavenumber of the RNL model to one determined mode improves its prediction. But it is not considered in the present study since it is not convenient for our finite-difference solver. Our results also indicate that increasing the grid resolution in the streamwise direction will ameliorate this phenomenon. However, it still differs from that of DNS even though the same N_x is used. Despite these differences, the Reynolds shear stress profiles predicted by the RNL model are quite realistic and close to those of DNS, as seen in figure 3 even at a higher Reynolds number of $Re_\tau = 950$. This makes it possible to use the RNL model as a physical reduced-order model to predict the drag economically. Since increasing N_x improves the prediction of Reynolds shear stress only slightly, hereafter, we will still use the grid numbers in table 1 for the RNL simulation. Due to the limitation of the streamwise wavenumbers, compared with DNS, grid numbers of the RNL model are decreased by a factor of 3.2, 8 and 32 at $Re_\tau = 100, 180, 950$, respectively. The corresponding CPU time for a single computational time step of RNL cases are 2.6, 5.5 and 31.2 times smaller than those of DNS cases based on the present numerical method. Also, it is noteworthy that by solving the governing equations of the RNL model in a hybrid physical/Fourier space

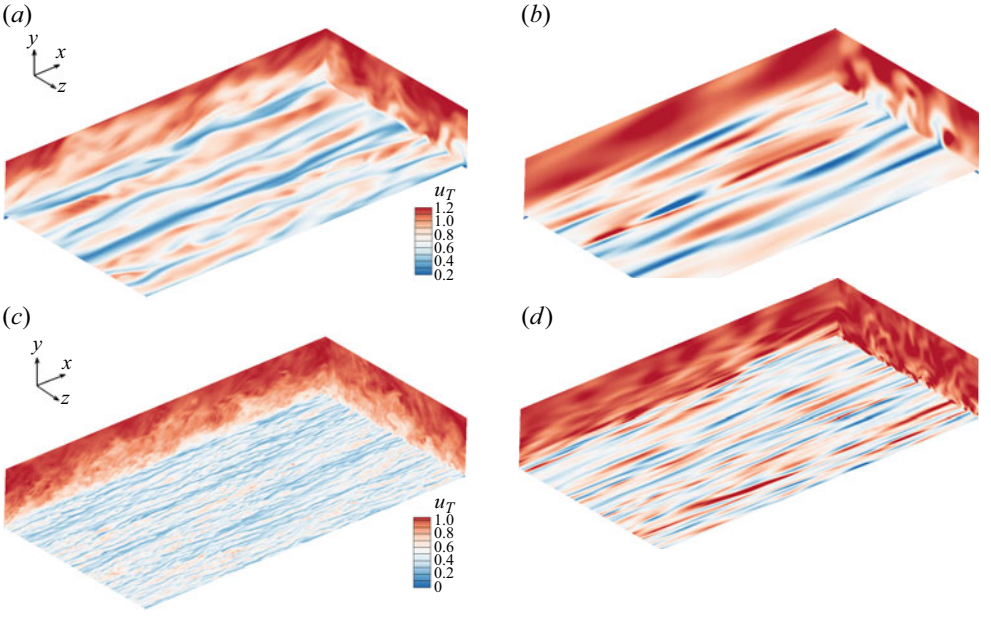

Figure 4. Comparison of the instantaneous streamwise velocity between DNS (*a*,*c*) and the RNL model (*b*,*d*): (*a*,*b*) $Re_\tau = 180$ and (*c*,*d*) $Re_\tau = 950$. The horizontal plane is at a wall distance of $y^+ = 15$.

grid with certain operations performed efficiently in Fourier space, the computational efficiency of the RNL model can be further improved (Bretheim, Meneveau & Gayme 2018).

Comparisons of the instantaneous flow field between DNS and the RNL model in figure 4 show there is a visible restriction of the streamwise wavelengths. However, from the cross-stream snapshot, the realistic vortical structures are obtained, which verifies the potential of the RNL model to reflect flow structures that are important in wall turbulence (Gayme & Minnick 2019). Since N_y, N_z are the same as those of DNS, even though the high- and low-speed streaks are elongated and much more straight in the streamwise direction, the number and distribution of the streaky structures in the spanwise direction are accurately predicted by the RNL model. Detailed comparisons between DNS and the RNL model of other physical quantities are presented in Appendix B, such as the instantaneous normal velocity, contours of the streamwise vorticity and so on.

Furthermore, the weights of the RNL-SL control model are trained through the data of RNL flow fields instead of DNS. So, it is necessary to compare the relationship between the velocity on the detection plane and the wall shear stresses in DNS and RNL flow fields. Figure 5 shows the contours of the two-point correlation coefficient ρ between $v_{y^+=10}$ and $\partial u/\partial y|_w$, $\partial w/\partial y|_w$ in both DNS and the RNL model at $Re_\tau = 180$ and $Re_\tau = 950$. In DNS flow fields it is shown that $v_{y^+=10}$ and wall shear stresses have distinct correlation in some regions. The correlation coefficients are antisymmetric with $\partial w/\partial y|_w$ and symmetrical with $\partial u/\partial y|_w$ in the spanwise direction. Also, the correlation with the spanwise wall shear rate is highest at slightly downstream, which is consistent with that of Park & Choi (2020). In RNL flow fields, distributions of the correlation coefficients are very similar to those in DNS flow fields. Limited to smaller streamwise computational grids, contours of the correlation coefficients are relatively straight in the streamwise direction. But in the spanwise direction, they share similar characteristics since the grid resolutions are the

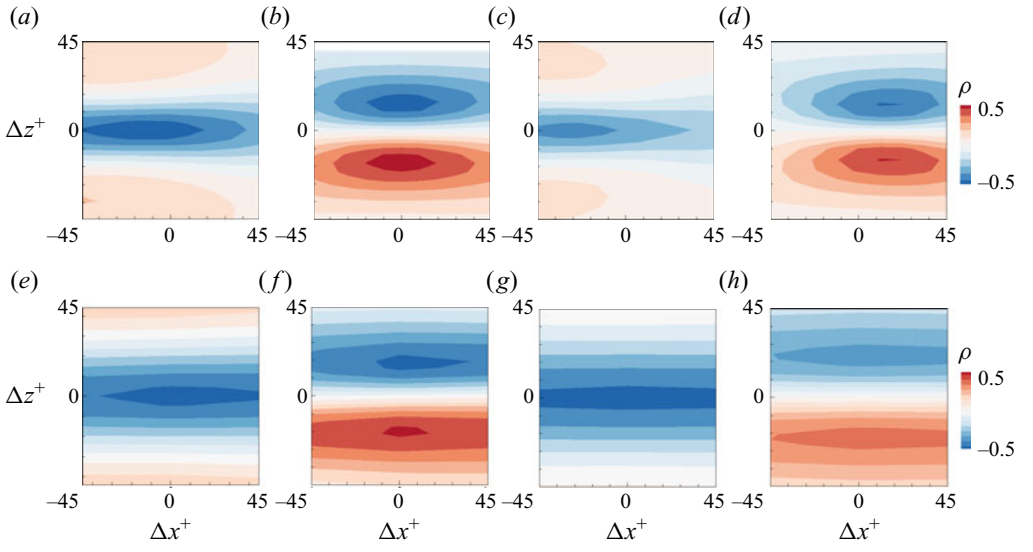

Figure 5. Contours of the correlation coefficients between $v_{y^+=10}$ and (*a*,*c*,*e*,*g*) $\partial u/\partial y|_w$, (*b*,*d*,*f*,*h*) $\partial w/\partial y|_w$. Results are shown for (*a–d*) DNS and (*e–h*) the RNL model at (*a*,*b*,*e*,*f*) $Re_\tau = 180$ and (*c*,*d*,*g*,*h*) $Re_\tau = 950$.

same as those of DNS. It shows that the RNL model accurately captures the relationship between the near-wall normal velocity and the wall shear stress, which makes it possible to apply machine learning control models trained by RNL data to control the real DNS field for drag reduction. Also, it is found that correlations of different Reynolds numbers are very similar in both DNS and the RNL model, indicating that machine learning control methods with similar structures are possible to be extended to high Reynolds numbers.

2.2. *The RNL-SL control framework*

Our previous study introduced the usage of CNNs for predicting wall actuations based on the streamwise or spanwise wall shear stress for drag reduction (Han & Huang 2020). As show in figure 6, the input data of CNN is wall shear stress and the output is the predicted wall blowing and suction. Based on the opposite control of Choi *et al.* (1994), the optimal wall actuations should have the same absolute value but opposite direction with the normal velocities at a detection plane. Here, the label data of CNN is opposite to the normal velocity at the detection plane, and the error between it and the output data is defined as the loss function, i.e.

$$\text{Loss} = \frac{1}{2}\sum_{i=1}^{N} \mathrm{e}^{\lambda|v^i_{label}|}(v^i_{label} - v^i_{output})^2, \tag{2.4}$$

$$v_{label} = -v_{y^+=10},\ v_{wall} = \sigma\, v_{output}, \tag{2.5}$$

to be minimized for updating the parameters of neural networks. In the above equations, λ is designed for emphasizing large wall actuations and chosen as 5 in this paper; v_{output} is the output of the CNN representing the predicted wall blowing and suction based on the wall shear stress. As introduced above, the amplitude of the wall blowing and suction is an important factor affecting the drag reduction rate. In the present study, considering that in a practical situation the controlled flow data are not available in

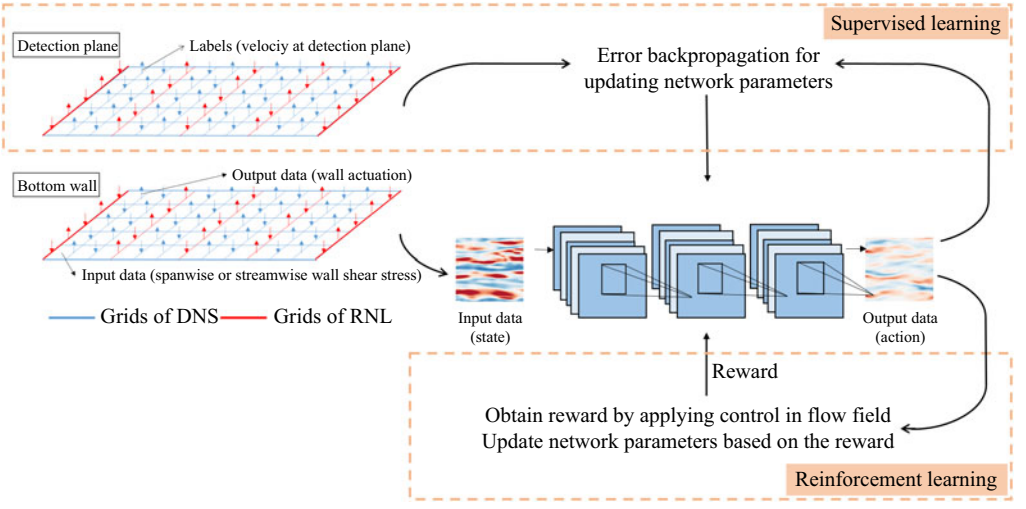

Figure 6. Schematic of the coupled RNL and machine learning control models.

advance, we train the RNL-SL control model from the uncontrolled RNL flow data. In that case, the root-mean-square (r.m.s.) value of v_{output} will be larger than that of $v_{y^+=10}$ in the opposition control case, because the near-wall normal velocity is obviously decreased in the controlled flow. According to Kim & Choi (2017), $v_{y^+=10,rms}$ (controlled) $\approx 0.5 v_{y^+=10,rms}$ (uncontrolled) under opposition control at $Re_\tau = 180$. It will be difficult to compare the present control effects with those of the traditional opposition control, as the amplitudes of the wall blowing and suction are different. So, σ in (2.5) is used to regulate the control strength at each control time step to ensure that $v_{wall,rms}$ is equal to $v_{y^+=10,rms}$ on the detection plane, i.e. $\sigma = v_{y^+=10,rms}$ (controlled) $/v_{output,rms}$, where $v_{y^+=10,rms}$ (controlled) is obtained in advance from the opposition control as a reference case.

Training data of the inputs and labels are both obtained from DNS in Han & Huang (2020). At higher Reynolds numbers, the training process of CNN will be observably elongated because a larger number of training data are required with the increasing complexity of the nonlinear relationship between the wall shear stress and normal velocities, which also causes an extra cost of obtaining training data. So it is harder and more expensive to extend it to a much more complicated flow situation with higher Re. The highest friction Reynolds number in Han & Huang (2020) and Park & Choi (2020) is 390 and 578, respectively. Furthermore, previous researches have revealed that the computational cost of neural networks is quite small compared with that of the flow solver. So, a scientific reduced-order model for calculating the flow field is necessary to accelerate the training process of the machine learning control model and extend the scope of its application to higher Re.

To the best of our knowledge, the RNL model has not been reported to be used for flow control problems. As seen above, the RNL model can reproduce the basic flow characteristics of turbulent channel flow to some extent with restricted streamwise Fourier components, which can easily simplify the flow representation. In this paper we apply the RNL model to drag reduction in wall turbulence coupled with machine learning technologies. The architecture of the RNL-SL control model is similar to that of the CNN control model proposed by Han & Huang (2020). The essential difference lies in the

training data of CNN. To reduce the computational cost and training difficulty, we exploit RNL simulation to obtain the training dataset including the input and label data instead of DNS. As seen in figure 6, the grids of the RNL model in the wall-normal and spanwise directions are kept the same as DNS, but the streamwise grids are limited to a few. All the training procedures are based on RNL data. When the loss function converges to the minimum, the training process of the CNN is finished, in which case the RNL-SL control model is equipped with the ability of predicting the normal velocity at the detection plane based on the wall shear stress of the RNL field. Then, it will be directly applied to the DNS flow, which is an absolutely new situation that the machine learning control model has never met. Based on the similarity of the flow field between the RNL model and DNS, the trained RNL-SL model should also be effective in controlling the realistic DNS field. We will first check its ability to predict the wall blowing and suction based on the wall shear stress and then investigate its drag reduction control effects on the real channel flow.

In the present study we also use two kinds of wall variables: streamwise and spanwise wall shear stresses, $\partial u/\partial y|_w$, $\partial w/\partial y|_w$, as the input data. Since Lee *et al.* (1998) have used a theoretical method to deduce the suboptimal control method, which obtains a concise formula describing the relationship of wall blowing and suction and spanwise wall shear stress, it is convenient to compare the control model based on RNL-SL with the analytical expression of suboptimal control method. For facilitating comparison, CNN with spanwise wall shear stress as input is constructed using a single linear convolutional layer without an activation function, and the size of the filter kernel in the streamwise direction is truncated to 1. This means that the CNN only has trainable weights in the spanwise direction. The size of the convolution kernel in the spanwise direction is determined based on previous knowledge (Lee *et al.* 1997; Han & Huang 2020; Park & Choi 2020) that at least approximately 90 wall units are necessary for $\partial w/\partial y|_w$ to predict the wall blowing and suction. It is noted that the performance of nonlinear CNN models is also tested with multiple convolutional layers and the hyperbolic tangent activation function. The results show that they do not significantly increase the drag reduction rate, indicating that a linear model is able to represent the relationship between $v_{y^+=10}$ and the spanwise wall shear stress.

For $\partial u/\partial y|_w$, theoretical derivation of the suboptimal control method fails due to the oversimplification of the strong nonlinear relationship between $\partial u/\partial y|_w$ and the normal velocities at the detection plane. We adopt a multi-layer nonlinear CNN architecture with a hyperbolic tangent activation function as the activation function. In this case, it is inevitable to involve the information of $\partial u/\partial y|_w$ in the steamwise direction when calculating the wall blowing and suction. However, the grids in the streamwise direction are much more sparse than DNS. In order to make the CNN structure trained based on RNL data directly adapted to DNS, before training, the training data from the RNL model is interpolated in the streamwise direction to share the same grid numbers as those of DNS. The computational cost of this interpolation is negligible. Our results also verify that the style of interpolation, such as linear, polynomial interpolation or padding zero for the energy of the larger wavenumber, has little influence on the training results, so hereafter the linear interpolation is used for convenience.

Architecture of the CNN used in the present study is shown in figure 7. Input data are the wall shear stress with the shape of $N_x \times N_z$. One convolutional layer used here includes periodic padding, convolutional operation, batch normalization and activation function. Due to the size of the filter kernel used in convolution, we use periodic padding in both the streamwise and spanwise directions to avoid the loss of edge information. We use the hyperbolic tangent activation function instead of rectified linear units (ReLU)

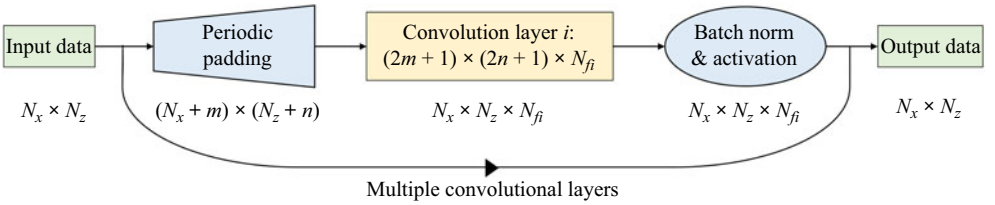

Figure 7. Architecture of the CNN used in the present study. Here $(2m + 1) \times (2n + 1)$ is the size of filter kernel and N_{fi} represents the number of filter kernels used in the ith convolutional layer. The output dimensions of each layer are shown below them. The widths of periodic padding in the streamwise and spanwise directions (m, n) are determined by the shape of the filter kernel to ensure that the output dimensions after convolution remain consistent with the input.

Input data	Re_τ	Number of convolutional layers	Size of filter kernel	Number of filter kernels	Activation function
	100	1	1×9	1	no
$\partial w/\partial y\|_w$	180	1	1×19	1	no
	950	1	1×19	1	no
	100	3	3×3	6,6,6	tanh
$\partial u/\partial y\|_w$	180	4	5×5	6,6,6,6	tanh
	950	5	9×9	6,6,6,6,6	tanh

Table 2. Details of the CNN architectures for different cases.

that is commonly used in CNN (Nair & Hinton 2010), in order to retain negative neural input and output in the training process. The corresponding hyperparameters of the CNN architecture are summarized in table 2, which are chosen based on our previous attempts based on DNS data (Han & Huang 2020).

2.3. *The RNL-RL control framework*

Even though prediction of the optimal wall blowing and suction by the RNL-SL model only requires the input of wall shear stress, its training process is dependent on the velocity within the flow field. In this section we combine the RNL model with RL, which undergoes training without reliance on labelled data. Due to the computational efficiency of the RNL model, we will further explore the potential of applying the RNL-RL control model to turbulent channel flows at higher Reynolds numbers.

As shown in figure 6, comparing with the RNL-SL model, it is seen that with the help of the RL architecture that updates the network parameters based on the reward of applying the RL output (action) to control the flow instead of the error between output and the label data, the RNL-RL model eliminates the dependence of information on the detection plane. The RL depends on a well-designed reward for better exploration of the unknown output region to optimize the weights of its neurons. The training datasets of the RL model, including the input data (state), the output data (action) and the reward of applying this action to control the turbulent channel flow, are acquired after each interaction between the RL control and the flow field. So, each interaction needs a numerical simulation of several time steps. Due to the lack of label data to guide the training, the RL model needs to observe the flow environment and adjust its action repeatedly within several epochs in order to obtain a larger reward. When one epoch finishes, the flow environment will

be reset and the next epoch of training begins. In each epoch with a time period of T, the RL agent described by CNN gets the state (s_t, defined as the wall shear stress) from the initial environment as input data, which is an instantaneous field of fully developed turbulent channel flow. After the operation of CNN, the RL agent outputs the action (a_t), which is thought to be the optimal wall blowing and suction based on the present CNN parameters. Then, the controlled RNL channel flow by a_t is advanced within a state step, which contains 50 simulation time steps according to Lee *et al.* (2023). Then the next state (s_{t+1}) is reached. In the present study, one epoch of RL T involves 800, 1200 and 2000 state steps at $Re_\tau = 100, 180, 950$, respectively. The reward of a state step is defined as

$$r_t = \frac{\overline{\tau_0} - \overline{\tau_w}}{\overline{\tau_0}}, \tag{2.6}$$

where $\overline{\tau_w}$ and $\overline{\tau_0}$ denote the averaged frictions with and without control within a state step, respectively. The training set (s_t, a_t, r_t, s_{t+1}) of one state step is then recorded into a replay buffer, whose memory size is chosen as 30 000, and when the replay buffer is full, the oldest data will be removed. During the training process, a group of training sets is chosen randomly from the replay buffer to decrease the correlation between them over time. The batch size is set to 64, which is determined based on previous knowledge.

The RL model used in the present study is trained by the deep deterministic policy gradient (DDPG) algorithm (Lillicrap *et al.* 2015), which is especially useful in continuous action problems. The DDPG consists of two networks: the actor network (μ_{θ^μ}) and the critic network (Q_{θ^Q}). The actor network is responsible for generating the output action based on the observed state, as mentioned earlier. Specifically, the output action is obtained using the equation $a_t = \mu_{\theta^\mu}(s_t)$. On the other hand, the critic network aims to evaluate the action by fitting a value function $Q_{\theta^Q}(s_t, a_t)$. This value function represents the expected return after taking the action a_t in the state s_t, i.e.

$$Q_{\theta^Q}(s_t, a_t) = \mathbb{E}\left[\sum_{i=t}^{T} \gamma^{i-t} r(s_i, a_i)\right], \tag{2.7}$$

where $\mathbb{E}$ means the expectation and γ is the time discount rate indicating the decaying effect of the action over time until the end of the epoch, which is chosen as 0.99 according to Fan *et al.* (2020*b*), Paris, Beneddine & Dandois (2021). Here θ^μ and θ^Q are the parameters of actor and critic networks; θ^μ is optimized by maximizing the expected total reward Q_{θ^Q} and θ^Q is updated based on the temporal difference error defined as the difference between the estimated value function of the current state-action pair and the value function of the next state-action pair. More details can be found in Appendix D.

The CNN architecture and its corresponding hyperparameters used in the actor network are the same as discussed in figure 7 and table 2, since their input and output are the same. The key to successful training of RL is based on a better estimate of the value function interpreted by the critic network. Referring to Lee *et al.* (2023), we use a relatively complex network as shown in figure 8. Different from the actor network based on figure 7, input of the critic network includes both the state and its corresponding action calculated from the actor network. The output of the critic network is the value of Q_{θ^Q}, which is utilized to assess the desirability of the action in the current state. Here, zero padding is used before each convolutional layer for simplicity. Due to substantial dimension reduction from input to output, average pooling is incorporated into certain convolutional layers and a fully connected layer is added before the output. The hyperparameters of the critic network are given in table 3.

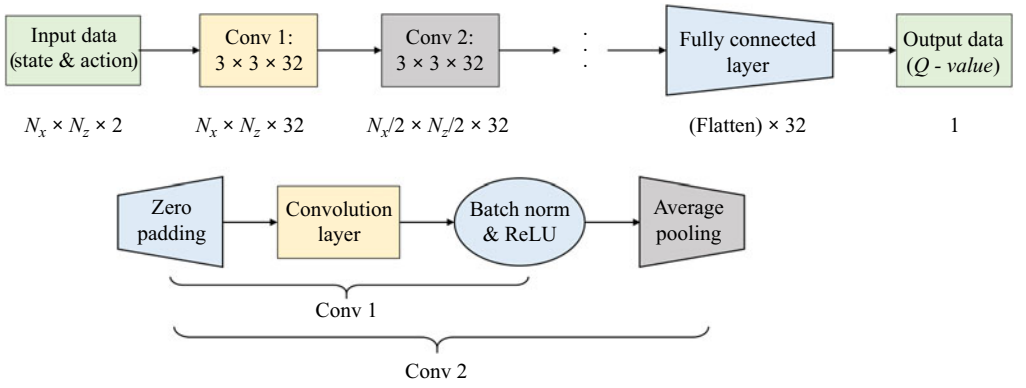

Figure 8. Architecture of the critic network used in DDPG. The output dimensions of each layer are shown below them. Conv 1 and Conv 2 represent two kinds of convolutional layers. Conv 2 has an additional average pooling layer compared with Conv 1.

Re_τ	Number of Conv 1	Number of Conv 2	Size of filter kernels	Number of filter kernels	Activation function
100	4	1	3×3	32	ReLU
180	3	2	3×3	32	ReLU
950	3	2	3×3	32	ReLU

Table 3. Hyperparameters used in the critic networks for different cases. Here, numbers of the filter kernels in each convolutional layer are all fixed as 32. The order Conv 1 + Conv 2 + (Conv 1) × 3 is used at $Re_\tau = 100$. The order (Conv 1 + Conv 2) × 2 + Conv 1 is used at $Re_\tau = 180, 950$. It is noted that these hyperparameters remain the same for both $\partial w/\partial y|_w$ and $\partial u/\partial y|_w$.

3. Training process and control result of RNL-SL model

In this section we show the training process of the RNL-SL model based on the data from the RNL flow field. Then its prediction performance in predicting the normal velocities on the detection plane based on the wall shear stress in both RNL and DNS flow fields is estimated. Active control results of the well-trained RNL-SL in DNS flow fields are presented subsequently.

3.1. *Training process*

There are three kinds of variables of RNL data: streamwise mean, fluctuation and their summation, based on which, the RNL-SL model can be trained separately when using $\partial w/\partial y|_w$ as input. For $\partial u/\partial y|_w$, given the demand of streamwise information of physical quantities, streamwise mean variables cannot be used for training. Since their training processes are almost the same, we only show the results based on the total (summation) quantities of RNL data. The training dataset consists of 2000 instantaneous RNL fields including the instantaneous wall shear stress and the corresponding normal velocities on the detection plane at $y^+ = 10$. The amount of training data is sufficient thanks to the characteristics of weight sharing of CNN architecture, because the output at each grid point of a convolutional layer is calculated using the same filter kernal for convolution operation. Figure 9 shows the averaged loss and correlation coefficient between the output and label data over each training epoch. It is obvious that all the losses decrease rapidly with epoch

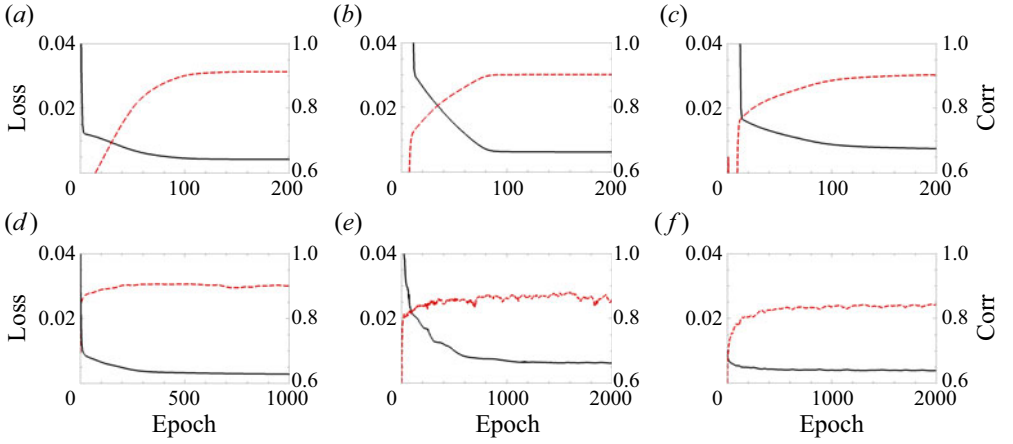

Figure 9. Training loss (black lines) and correlation coefficient (red dashed lines) between the output and label of the RNL-SL model in terms of epoch based on the input of (*a–c*) $\partial w/\partial y|_w$ and (*d–f*) $\partial u/\partial y|_w$: (*a*,*d*) $Re_\tau = 100$, (*b*,*e*) $Re_\tau = 180$, (*c*,*f*) $Re_\tau = 950$.

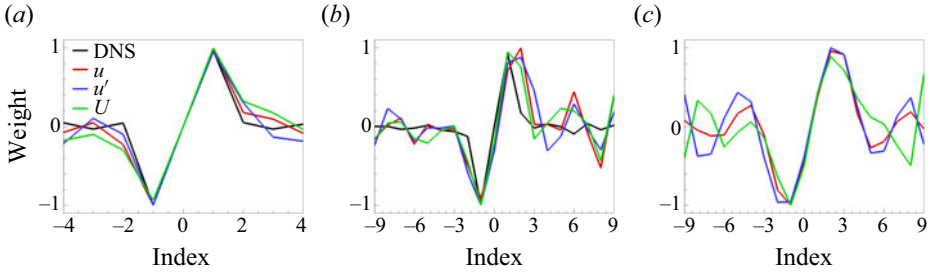

Figure 10. Weight distribution in the spanwise direction of the RNL-SL model based on $\partial w/\partial y|_w$ from (*a*) $Re_\tau = 100$, (*b*) $Re_\tau = 180$, (*c*) $Re_\tau = 950$. The model is trained based on the total velocity ($\boldsymbol{u}$), fluctuation velocity ($\boldsymbol{u}'$) and mean velocity ($\boldsymbol{U}$) from the RNL model and compared with that from DNS.

and eventually achieve a convergent value. Variations of the correlation coefficients exhibit the same variation tendency. All the correlation coefficients are around 0.90, indicating great interpretation of the relationship between wall shear stresses and the normal velocity on the detection plane by the RNL-SL model. It also shows that the number of training epochs of $\partial u/\partial y|_w$ is almost 10 times larger than that of $\partial w/\partial y|_w$ because of the complexity of their CNN architectures. The fluctuations of the loss and correlation coefficient of $\partial u/\partial y|_w$ are much larger, implying the complex nonlinear relations between the input and output of CNN, making it difficult for training. However, when comparing the training processes of $Re_\tau = 180$ with that of $Re_\tau = 950$, it is found that the necessary epochs do not increase distinctly with Reynolds number for both $\partial w/\partial y|_w$ and $\partial u/\partial y|_w$.

Due to the simple architecture of CNN for $\partial w/\partial y|_w$, we can easily draw out the distribution of the filter kernels in the spanwise direction in figure 10. We compare the models trained with three different kinds of RNL data as mentioned above as well as the weights obtained based on DNS data from Han & Huang (2020), which have been proved perfectly consistent with the theoretical solution of suboptimal control. It is surprising that the weight distributions of all the cases are analogous with each other. Weights near the point of interest have the largest value and then decay rapidly to almost zero at the boundary of the sensing region of the filter kernel. It is worth noting that the weight

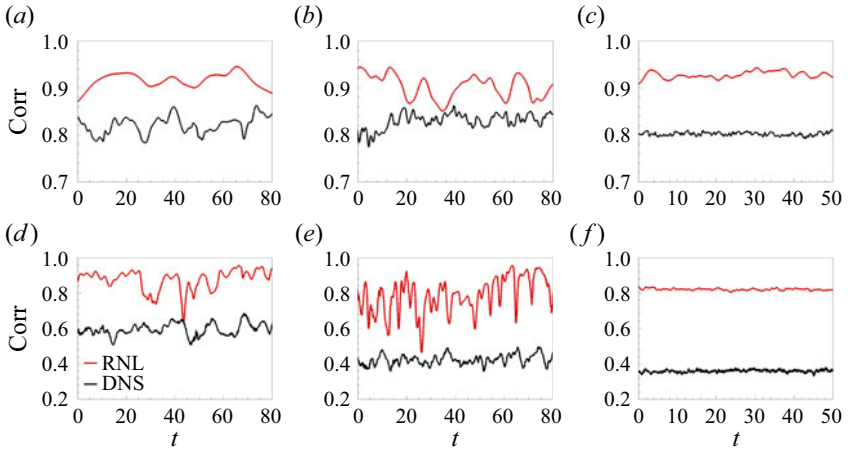

Figure 11. Test results of the correlation coefficient between the output and the label of the RNL-SL model in terms of time based on the input of (*a–c*) $\partial w/\partial y|_w$ and (*d–f*) $\partial u/\partial y|_w$: (*a*,*d*) from $Re_\tau = 100$, (*b*,*e*) from $Re_\tau = 180$, (*c*,*f*) from $Re_\tau = 950$. Results are compared between DNS and the RNL model by using the same model trained by RNL data.

distributions do not demonstrate strict antisymmetry as observed in the analytical solutions of the suboptimal control, even though we attempted to triple the size of the training data. But it has only a small influence on the drag reduction effect, indicating that the training data are sufficient and the training process is converged. The results of $Re_\tau = 950$ have not been shown in previous studies, but the similar distribution profile and good prediction performance shown below verifies their credibility. Successful training of the CNN model based on RNL data reveals that the RNL simulation makes a reliable prediction of the turbulent channel flow, especially in the near-wall region.

3.2. *Comparison of prediction performance in the RNL model and DNS*

To illustrate the prediction performance of the trained RNL-SL models, we apply them to both RNL and DNS flow fields, which are new for them to test. The time histories of the correlation coefficients at the steady stage in the RNL model and DNS are shown in figure 11. For $\partial w/\partial y|_w$, the predicted correlation coefficients of the RNL model at different Reynolds numbers almost remain constant without decaying with time. Their averaged values are all around 0.9, which are nearly the same as those of the training process. It indicates that the RNL-SL model is well trained and can effectively reflect the relationship between wall shear stress and the predicted wall blowing and suction. When directly applying the RNL-SL model to the DNS flow field, the correlation coefficients obtained are a little smaller than those in the RNL test flow field. However, the averaged values are still over 0.8, which is larger than that using other machine learning methods, e.g. the Lasso (Tibshirani 1996), random forest (Breiman 2001) and fully connected neural networks as discussed in Park & Choi (2020). For $\partial u/\partial y|_w$, it is observed that there appears to be a more distinct oscillation of the correlation coefficient than that in the training process. However, the averaged values of the RNL flow field are almost kept at a similar level close to the training cases, which are about 0.9, 0.8 and 0.8 at $Re_\tau = 100$, 180, 950, respectively. The correlation coefficients in the DNS test field decline sharply to 0.6, 0.4 and 0.38 as compared with those in the RNL field. Differences of the prediction performance in the RNL model and DNS for $\partial u/\partial y|_w$ can be attributed to deficiency of the flow field details

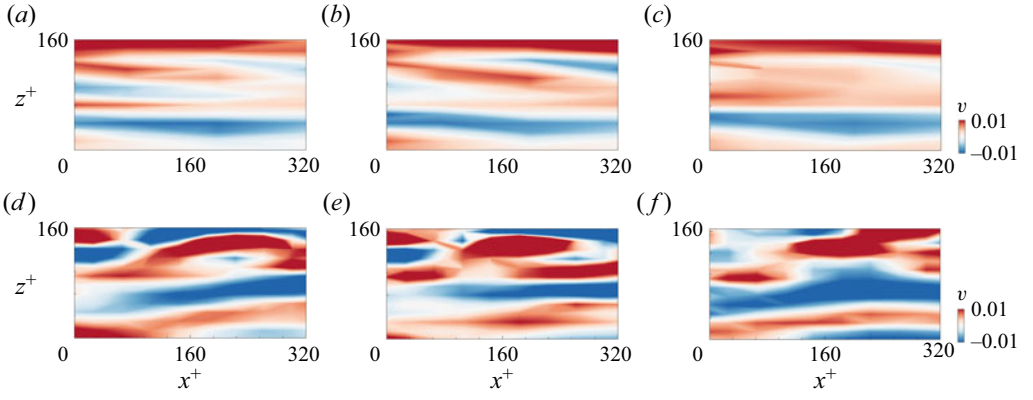

Figure 12. Instantaneous contours of v_{label} and v_{wall} at $Re_\tau = 100$: (*a*,*d*) v_{label}, (*b*,*e*) v_{wall} based on $\partial w/\partial y|_w$, (*c*,*f*) v_{wall} based on $\partial u/\partial y|_w$. Plots (*a–c*) are from the RNL model and (*d–f*) are from DNS.

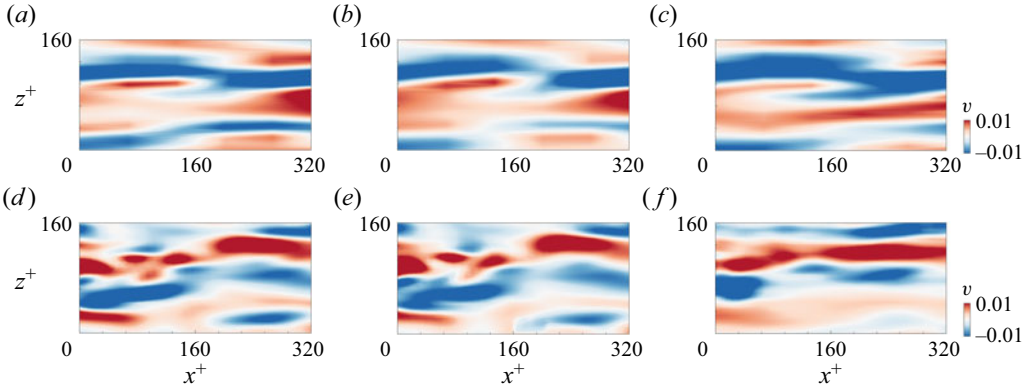

Figure 13. Instantaneous contours of v_{label} and v_{wall} at $Re_\tau = 180$: (*a*,*d*) v_{label}, (*b*,*e*) v_{wall} based on $\partial w/\partial y|_w$, (*c*,*f*) v_{wall} based on $\partial u/\partial y|_w$. Plots (*a–c*) are from the RNL model and (*d–f*) are from DNS.

in the streamwise direction, which is necessary for predicting the normal velocities from $\partial u/\partial y|_w$. Nevertheless, these coefficients are stable without changing with time.

Figures 12–14 show the instantaneous prediction results based on the RNL-SL models in both the RNL and DNS flow fields at different Reynolds numbers. Due to the restriction of the streamwise modes in the RNL model, the contours of the normal velocities at $y^+ = 10$ show elongated features (figures 12–14*a*), which can also be seen in the prediction results (figures 12–14*b*,*c*). It is also seen that the performances of $\partial w/\partial y|_w$ always outperform those of $\partial u/\partial y|_w$, consistent with the correlation coefficients in figure 11. Figures 12–14(*e*,*f*) are obtained directly by using the corresponding RNL-SL model in the DNS flow field. Despite the substantial differences between the labels from the RNL model and DNS (comparing figures 12–14(*a*) with (*c*)), the RNL-SL models are also effective for prediction. It is not difficult to infer that the control model trained only based on RNL data can give a good prediction of the velocity field in the spanwise direction, because the RNL model and DNS have the same spanwise computational domain and grid resolution. On the other hand, the prediction performance based on $\partial w/\partial y|_w$ is much better than that of $\partial u/\partial y|_w$. It is not only because of the simple relationship between $\partial w/\partial y|_w$ and v at $y^+ = 10$, but also because the CNN model based on $\partial w/\partial y|_w$ does not

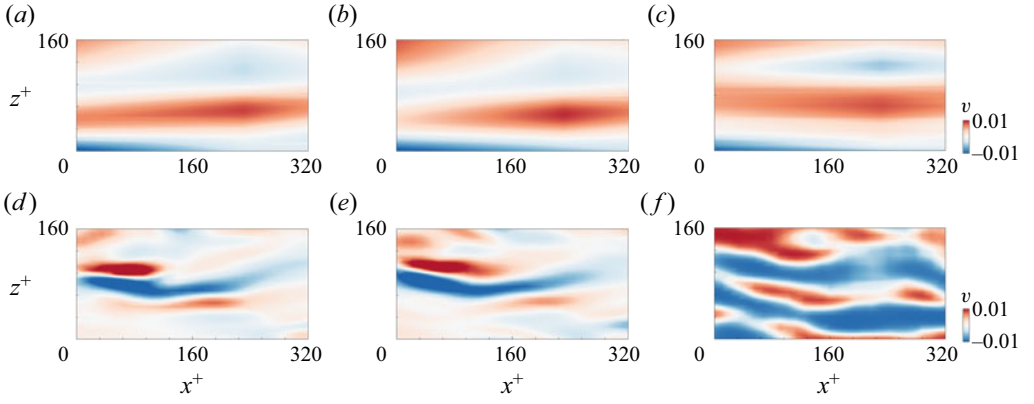

Figure 14. Instantaneous contours of v_{label} and v_{wall} at $Re_\tau = 950$: (*a*,*d*) v_{label}, (*b*,*e*) v_{wall} based on $\partial w/\partial y|_w$, (*c*,*f*) v_{wall} based on $\partial u/\partial y|_w$. Plots (*a–c*) are from the RNL model and (*d–f*) are from DNS.

	Averaged correlation coefficients based on	
Re_τ	$\partial w/\partial y\|_w$	$\partial u/\partial y\|_w$
100	0.85	0.55
180	0.85	0.36
950	0.81	0.30

Table 4. Averaged correlation coefficients between the output of the RNL-SL model and the normal velocities at $y^+ = 10$ of the controlled DNS flow based on the streamwise and spanwise wall shear stresses at $Re_\tau = 100, 180, 950$.

need the streamwise direction information and the model based on $\partial u/\partial y|_w$ is influenced by information in the streamwise direction, especially when using a larger number of convolution layers. According to table 1, in order to reduce the computational cost, fewer grids in the streamwise direction are used and the ratio of N_z to N_x becomes larger with Reynolds numbers. When training the RNL-SL model at a larger Reynolds number, the deficiency of the flow simulation in the streamwise direction becomes more evident. Lack of some effective and key information makes it perform not so well as that using the spanwise wall shear stress. However, the flow features in the spanwise direction, such as the alternating positive and low-speed streaky structures are evident and similar to the label data.

3.3. *Application to active control*

In this subsection we apply the well-trained RNL-SL models by the uncontrolled RNL data to DNS flow fields for drag reduction in a turbulent channel flow at different Reynolds numbers. Table 4 shows the averaged correlation coefficients between the predicted wall blowing and suction and the normal velocities at the detection plane in the controlled DNS flow. Comparing these results with those shown in figure 11, it can be concluded that based on $\partial w/\partial y|_w$, the trained RNL-SL models perform well for prediction in both the uncontrolled and controlled flow fields, and their correlation coefficients are almost the same. Based on $\partial u/\partial y|_w$, the averaged correlation coefficients decrease as compared with

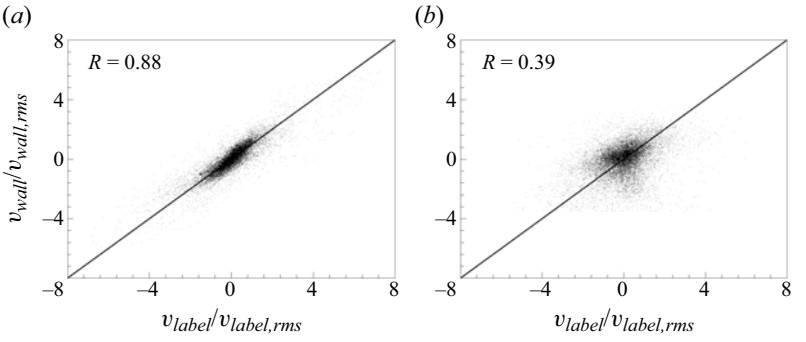

Figure 15. Scatter plots of v_{label} and v_{wall} at $Re_\tau = 180$ based on (*a*) $\partial w/\partial y|_w$ and (*b*) $\partial u/\partial y|_w$.

that based on the uncontrolled flow data, indicating the influence of the wall blowing and suction on the relationship between streamwise wall shear stress and the normal velocities at $y^+ = 10$. This phenomenon was also detected by Park & Choi (2020), where the correlation coefficient is decreased more than that of the present study. The reason may be that they use a more complex CNN architecture for training. In the present study, since the streamwise modes of the RNL training data are substantially restricted, using a CNN model with more convolutional layers and filter kernels does not improve the training and prediction accuracies obviously. Even though the prediction performance in the controlled flow field is a little lower than that of the uncontrolled one, the predicted wall blowing and suction also maintain approximately linear relations with the labels as shown in figure 15 taken the cases of $Re_\tau = 180$, for example. The predicted wall blowing and suction can also reproduce the main flow characteristics of the flow field, as shown by the instantaneous contours in figure 16. The results are consistent with those in figures 12–14(*d–f*), where the RNL-SL models with input of $\partial w/\partial y|_w$ make a better prediction of not only the correlation coefficient of the whole flow field but also the details of the flow structures. When using $\partial u/\partial y|_w$ as input, the RNL-models' prediction capacity decreases and the predicted velocity distribution appears with nonconformity from the view within some small windows of the flow field, which explains the reason of lower drag reduction rates shown below.

Figure 17 presents the time histories of the wall shear stress of controlled flow based on $\partial w/\partial y|_w$ and $\partial u/\partial y|_w$ compared with the uncontrolled ones at different Reynolds numbers. The wall shear stress (τ_w) of the controlled case is normalized by the uncontrolled case (τ_0) at each Reynolds number. It is obvious that all the cases controlled by RNL-SL models obtain drag reduction and when the control begins at $t = 0$, the wall shear stress decreases immediately and reaches a new level with a lower skin friction. The time interval to reach this new level becomes shorter with the increase of Reynolds number. The drag reduction rate is defined as

$$DR = \frac{\tau_0 - \tau_w}{\tau_0} = 1 - \frac{\tau_w}{\tau_0}, \tag{3.1}$$

which is larger based on $\partial w/\partial y|_w$ than that of $\partial u/\partial y|_w$. This is consistent with the prediction performance as listed in table 4. Furthermore, to compare the drag reduction rates based on the RNL-SL model with those of the traditional opposition control, drag reduction rates of different cases are given in table 5. For the opposition control based on the normal velocities at $y^+ = 10$ of $Re_\tau = 180$, 20 % drag reduction is obtained, which is the same as those obtained in the previous studies (Chang *et al.* 2002; Chung & Talha

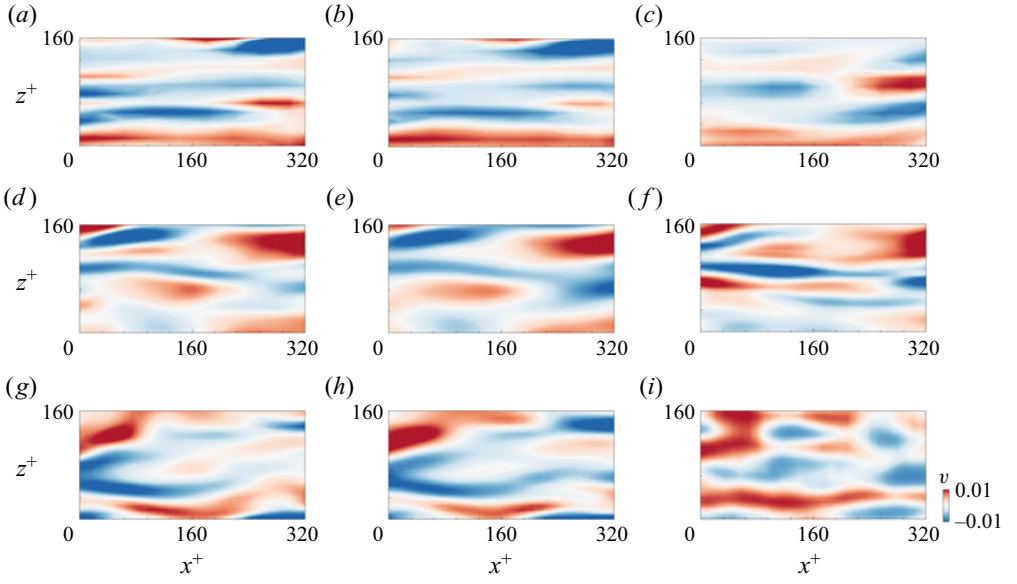

Figure 16. Instantaneous contours of v_{label} and v_{wall} from the controlled DNS flow field: (*a*,*d*,*g*) v_{label}, (*b*,*e*,*h*) v_{wall} based on $\partial w/\partial y|_w$, (*c*,*f*,*i*) v_{wall} based on $\partial u/\partial y|_w$. Plots (*a–c*) are from $Re_\tau = 100$, (*d–f*) are from $Re_\tau = 180$ and (*g–i*) are from $Re_\tau = 950$. The correlation coefficients of $Re_\tau = 100$, 180, 390 are 0.91, 0.88, 0.81 based on $\partial w/\partial y|_w$ and 0.52, 0.39, 0.36 based on $\partial u/\partial y|_w$, respectively.

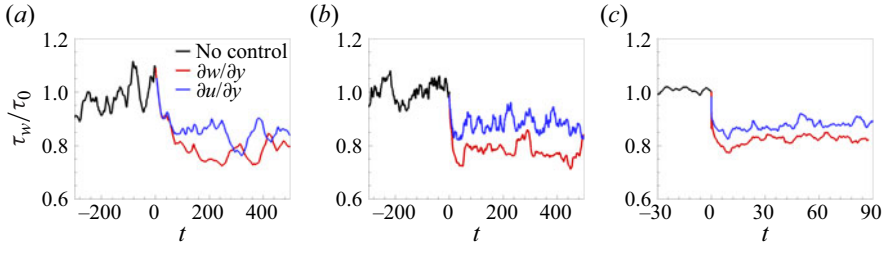

Figure 17. Time histories of the streamwise wall shear stress of uncontrolled and controlled flows based on $\partial w/\partial y|_w$ and $\partial u/\partial y|_w$: (*a*) $Re_\tau = 100$, (*b*) $Re_\tau = 180$ and (*c*) $Re_\tau = 950$.

Re_τ	DR (%) with the opposition control	DR (%) with RNL-SL	
		$\partial w/\partial y|_w$	$\partial u/\partial y|_w$
100	21	19	16
180	20	19	14
950	18	16	12

Table 5. Drag reduction rates (DR) from different cases of the RNL-SL model control and corresponding opposition control.

2011). So far few researches have reported the opposition control results for $Re_\tau = 950$; $DR = 18\,\%$ in the present study is close to the value of 16 % reported by Deng *et al.* (2016) for $Re_\tau = 1000$ at $y^+ \approx 9.8$ using a spectral DNS solver. Drag reduction rates of the RNL-SL models based on $\partial w/\partial y|_w$ can almost reach over 95 % of those based on the opposition control, which means that the wall blowing and suction predicted by $\partial w/\partial y|_w$

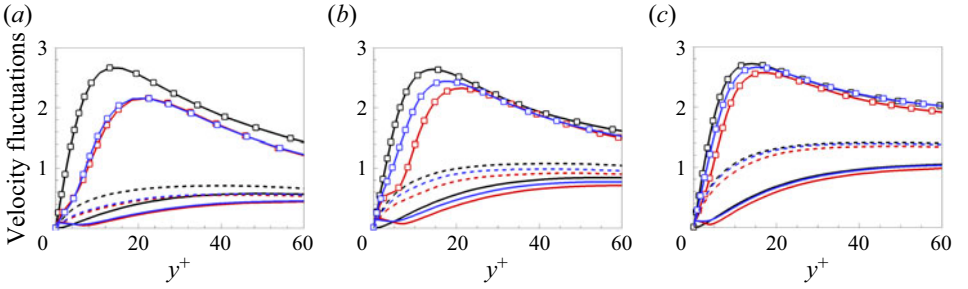

Figure 18. Profiles of the turbulent velocity fluctuations, u_{rms} (line with square), v_{rms} (solid line) and w_{rms} (dashed line) from cases of no control (black), controlled based on $\partial w/\partial y|_w$ (red) and $\partial u/\partial y|_w$ (blue): (*a*) $Re_\tau = 100$, (*b*) $Re_\tau = 180$, (*c*) $Re_\tau = 950$.

capture well the main characteristics of the optimal velocities on the detection plane. By means of the simplicity and computation economy of the RNL training data, the coupled RNL and CNN method can be easily applied to higher Reynolds numbers. Limited to the prediction performances of the RNL-SL models based on $\partial u/\partial y|_w$, drag reduction rates are always lower than that based on $\partial w/\partial y|_w$ at all the Reynolds numbers. But the drag reduction rates based on $\partial u/\partial y|_w$ are all over 12 % at different Reynolds numbers up to $Re_\tau = 950$, which is still larger than those reported in the previous studies, e.g. 10 % from a two-dimensional linear controller at $Re_\tau = 100$ (Lee *et al.* 2001), 12 % from a control scheme optimized by a genetic algorithm at $Re_\tau = 100$ (Morimoto *et al.* 2002), 11.5 % from an improved suboptimal control at $Re_\tau = 180$ (Fukagata & Kasagi 2004) and 11 % from a multiple input and output CNN controller at $Re_\tau = 180$ (Park & Choi 2020).

Figure 18 presents the profiles of the velocity fluctuations of the controlled channel flow and the uncontrolled one at different Reynolds numbers. All the components of the velocity fluctuations were substantially suppressed by the wall blowing and suction of the RNL-SL models, among which the suppression on the wall-normal velocity from the controller based on $\partial w/\partial y|_w$ is the most pronounced. Focusing on v_{rms}, it can be found that it has a value greater than 0 at the wall and is almost equal with that of $y^+ = 10$, which determines a similar control strength with that of the opposition method according to (2.5). The value v_{rms} decreases firstly and then increases with y^+. It forms a minimum value close to zero between the wall and $y^+ = 10$, where a 'virtual wall' is established to prevent the momentum and energy transfer, resulting in drag reduction (Hammond *et al.* 1998). Figure 19 shows the instantaneous vortical structures identified by using the second invariant of the velocity gradient tensor (Q). With the same value of Q, the controlled flow fields show fewer vortices compared with the uncontrolled cases, which verifies that the wall blowing and suction destroy the vortical structures. Furthermore, the degree of the weakening of the vortex is proportional to the drag reduction rate, which is consistent with the results shown in table 5.

4. Training process and control result of RNL-RL model

In this section the RL control of a turbulent channel flow based on the input of the wall shear stress only is investigated. In contrast to the RNL-SL control model, the training process of the RNL-RL model is online learning, which means that it is completed while continuously learning how to effectively control flow fields. The whole training process is carried out in RNL flow fields and the label data are not needed. Then, the well-trained RNL-RL model is also tested to control the DNS flow.

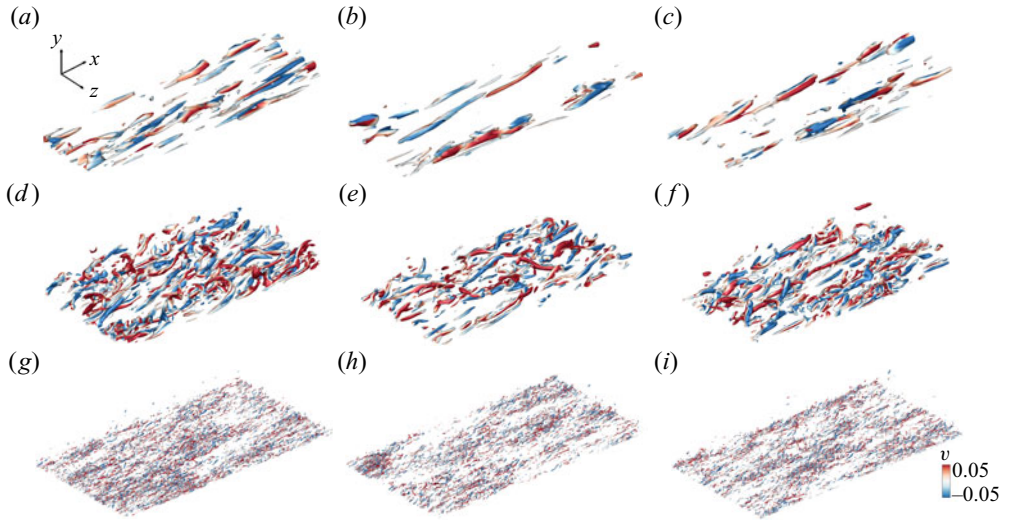

Figure 19. Instantaneous vortical structures identified by the isosurface of Q within the lower half-channel flow for uncontrolled cases (a,d,g), controlled cases based on $\partial w/\partial y|_w$ (b,e,h) and $\partial u/\partial y|_w$ (c,f,i). The vortical structures are coloured by the normal velocities. Results are shown for (a–c) $Re_\tau = 100$, $Q = 0.1$; (d–f) $Re_\tau = 180$, $Q = 1$; (g–i) $Re_\tau = 950$, $Q = 30$.

4.1. *Training process*

As described in § 2.3, RNL-RL discovers the optimal control strategy through iterative interactions with the flow field within a single epoch. When an epoch ends, the environment will be reset to the uncontrolled one and a new iteration of learning begins. Figure 20 shows the training process of the RNL-RL model based on the input of $\partial w/\partial y|_w$. The averaged reward within the second half-epoch increases rapidly with each epoch and is converged to a constant, indicating that the model has been well trained. The minimum number of training epochs is about 10 for all the cases at $Re_\tau = 100, 180, 950$. It is similar to that of 16 epochs trained through the DNS flow field at $Re_\tau = 180$, as reported by Lee *et al.* (2023). Due to the usage of the RNL model for training, the computational cost is over 10 times lower at the same Reynolds number of $Re_\tau = 180$. At $Re_\tau = 950$, the computational cost has fallen even more sharply (by over 30 times as shown in table 1) due to the fewer grids used in the streamwise direction, where $N_x = 16$ in the RNL model and $N_x = 512$ in DNS, for example. So, the present RNL-RL model can be easily extended to control the turbulent flow at a much higher Reynolds number. During the training process, we also monitor the correlation coefficient between the output of the RNL-RL model and the normal velocities on the detection plane. Figure 20(d,e,f) clearly shows that during the last five epochs of the training process of the RNL-RL model, the correlation coefficient at each state step remains around 0.8, which is similar to that of the test results of the RNL-SL model shown in figure 11. This result shows that the control strategy learned by RL based on $\partial w/\partial y|_w$ without label data also leads to a similar result with the opposition control method.

To learn more details about the training process, figure 21(a) shows the normalized wall shear stress of uncontrolled flow and the controlled flow by the RNL-RL model within the first 10 epochs. It can be found that at the beginning of training, the RNL-RL model fails to output effective wall blowing and suction, resulting in the increase of wall shear stress. However, the RNL-RL model continuously adjusts its control strategy within the

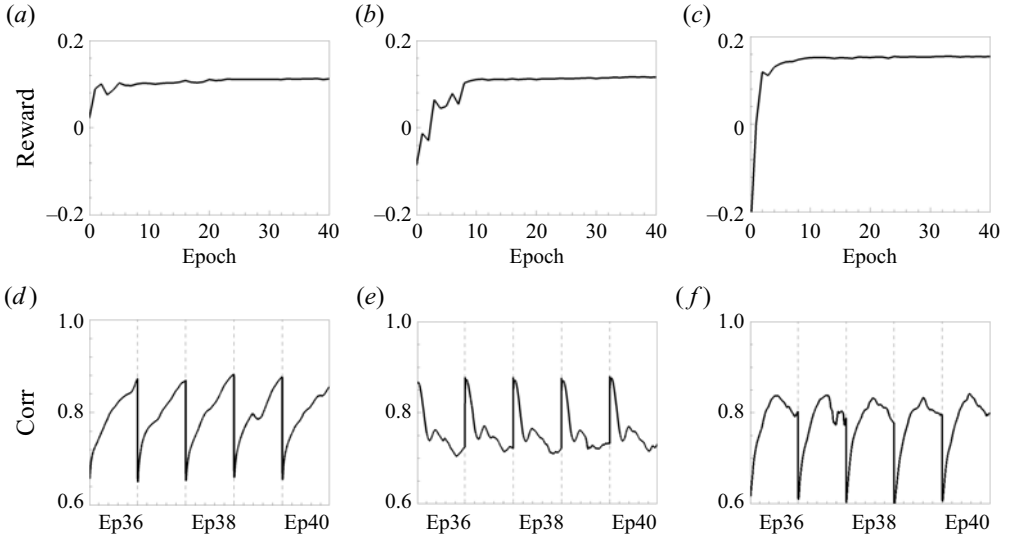

Figure 20. Reward (*a–c*) and the correlation coefficient (*d–f*) between the output of the RNL-RL model and the normal velocities at $y^+ = 10$ in terms of epoch based on the input of $\partial w/\partial y|_w$: (*a*,*d*) $Re_\tau = 100$, (*b*,*e*) $Re_\tau = 180$, (*c*,*f*) $Re_\tau = 950$.

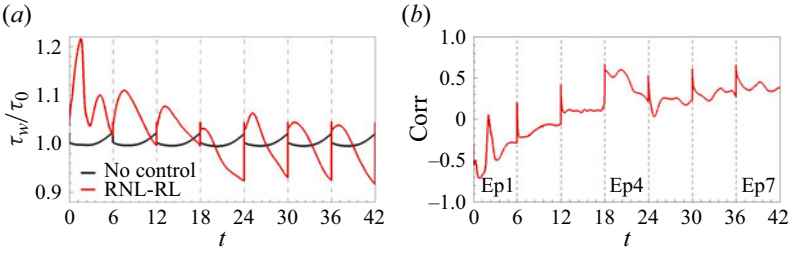

Figure 21. Wall shear stresses of the uncontrolled and controlled flows by the RNL-RL model (*a*) and the corresponding correlation coefficient between the output of the RNL-RL model and the normal velocity at $y^+ = 10$ (*b*) within the first 10 epochs at $Re_\tau = 180$.

following epochs and succeeds in reducing the friction at the wall. Also, the drag reduction rate increases with each epoch, showing better control performance. The corresponding correlation coefficient also appears to have a similar variation trend in figure 21(*b*).

Figure 22 compares the converged weight distribution of the RNL-RL model with that of the RNL-SL model. It is surprising that results agree well with each other, which means that the CNN, which describes the relation between $\partial w/\partial y|_w$ and the optimal wall blowing and suction determined by RNL-SL and RNL-RL models, shares the same weight distribution. In other words, the control strategy discovered from our RNL-RL model that only uses spanwise wall shear stress in RNL flow fields as input, is close to the globally optimal solution.

4.2. *Application to active control*

Even though the training process in RNL flow fields shows effective drag reduction, it still needs to test whether the RNL-RL model also works well in real DNS flow fields. Figure 23 shows the drag reduction results in a DNS test. It is notable that the drag

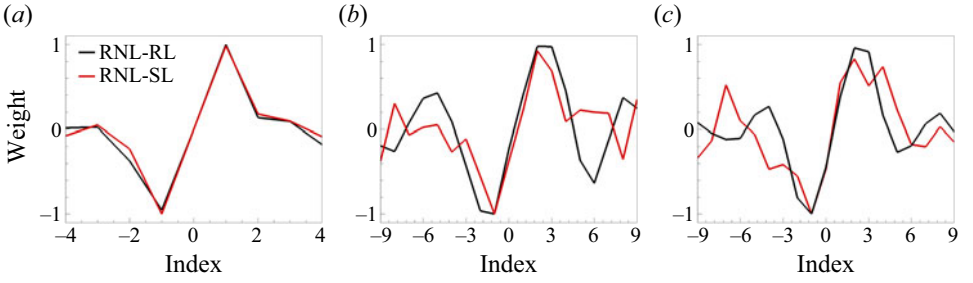

Figure 22. Weight distribution in the spanwise direction of the RNL-RL model based on $\partial w/\partial y|_w$ at (*a*) $Re_\tau = 100$, (*b*) $Re_\tau = 180$ and (*c*) $Re_\tau = 950$. The model is trained based on the total velocity ($\boldsymbol{u}$) and compared with the RNL-SL model.

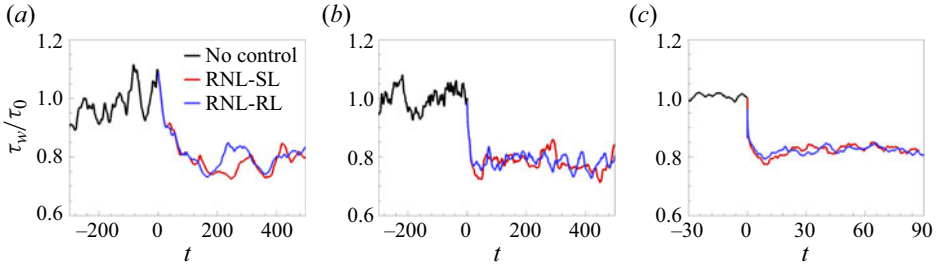

Figure 23. Comparison of time histories of the streamwise wall shear stress of uncontrolled and controlled flows based on $\partial w/\partial y|_w$ from the RNL-SL and RNL-RL models: (*a*) $Re = 100$, (*b*) $Re = 180$, (*c*) $Re = 950$.

reduction rate is larger than the convergent reward shown in figure 20. The reason is that during the period of each epoch, as shown in figure 21(*a*), the wall shear stress has not reached the steady stage. But it has no influence on the training of the RNL-RL model, because in this period of epoch, the model has been trained well enough and increasing the period will not improve the training effect. It has also been discussed in detail in Han *et al.* (2022) about the influence of T on the training results. Moreover, it is found that the drag reduction rates at different Reynolds numbers are almost the same as those of the RNL-SL models. According to table 5, drag reduction rates of our RNL-RL models also achieve 90 %, 95 % and 89 % of those with opposition control.

Furthermore, the control mechanism determined by RNL-RL is analysed and compared with that of the opposition control. The previous researches have shown that the spanwise wall shear stress is an indicator of the streamwise vortices, better than wall pressure and streamwise wall shear stress, because $\partial w/\partial y|_w$ is the spanwise trace left by the streamwise vortices on the wall and they show strong correlation in the near-wall region (Kravchenko *et al.* 1993; Ge, Xu & Cui 2011). Ge *et al.* (2011) further compared the differences of the cross-correlation coefficients between $\partial w/\partial y|_w$ and ω_x from the uncontrolled flow field and the controlled one by random wall blowing and suction. It was found that they almost remained the same as each other, which meant that the correlation between $\partial w/\partial y|_w$ and ω_x was robust and would not be affected by the wall actuations. In that case, by using $\partial w/\partial y|_w$ as the input, our RNL-RL model should also be able to detect the appearance of the streamwise vortices and determine wall blowing and suction for control.

To clarify this control mechanism, referring to Lee *et al.* (2023), we show the instantaneous contours of the streamwise vorticity and the wall blowing and suction in figure 24. From the most prominent blue region in figure 24(*a*) (representing a negative

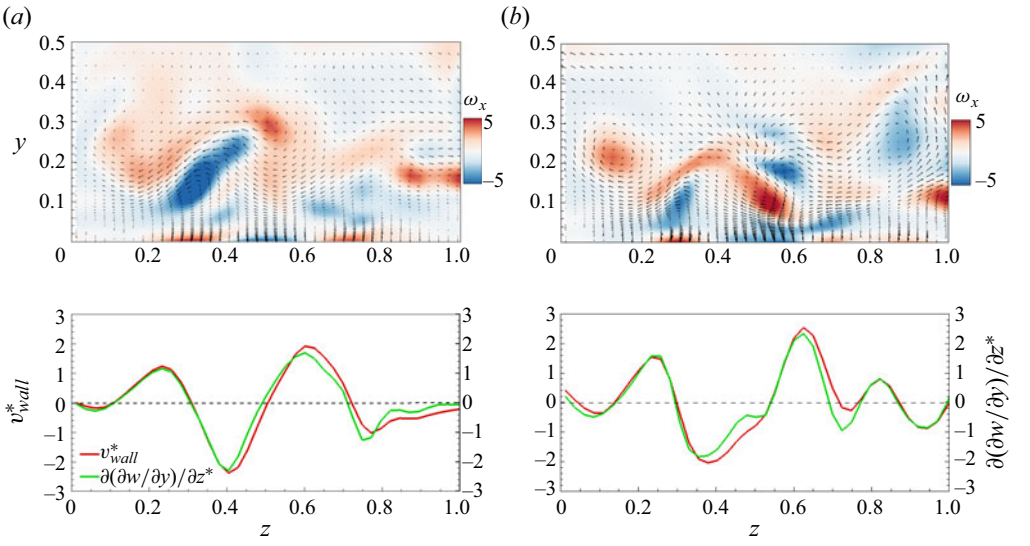

Figure 24. Instantaneous contours of the streamwise vorticity with v–w velocity vector field and the wall blowing and suction based on the RNL-RL model at $Re_\tau = 180$ at different times of (a,b). Lines of the z gradient of the spanwise wall shear stress ($(\partial/\partial z)/\partial w/\partial y|_w$) and the wall blowing and suction are compared. Here the asterisk represents normalization by the r.m.s. values of themselves.

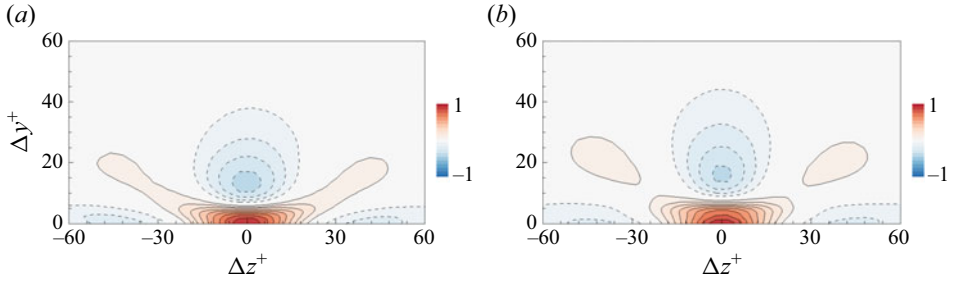

Figure 25. Contours of the two-point correlation between the spanwise wall shear stress and the streamwise vorticity in (a) uncontrolled and (b) controlled flow by the RNL-RL model at $Re_\tau = 180$.

streamwise vorticity), it is seen that sweep and ejection events are induced on the left and right sides, respectively. Within this region, the control strategy derived by RL involves applying blowing in the sweeping region and suction in the ejection region. This control strategy is similar with the opposition control and the suboptimal control based on $\partial w/\partial y|_w$, since both of them aim at suppressing the up-and-down motion induced by the streamwise vortices (Choi *et al.* 1994; Lee *et al.* 1998, 2023). The most prominent red region shown in figure 24(b) also exhibits a consistent drag reduction mechanism. Also, the effect of wall blowing and suction by the RNL-RL model on the near-wall turbulence is shown by the two-point correlation between the spanwise wall shear stress and streamwise vorticity in figure 25. It is found that these correlations are suppressed by the RNL-RL control and the position of the correlation minima appears further away from the wall, indicating the weakening of the streamwise vortices. So, it can be concluded that if only using $\partial w/\partial y|_w$ as input, RNL-RL tends to capture the streamwise vortices suppression mechanism as its optimal solution, which has also been reported by Lee *et al.* (2023).

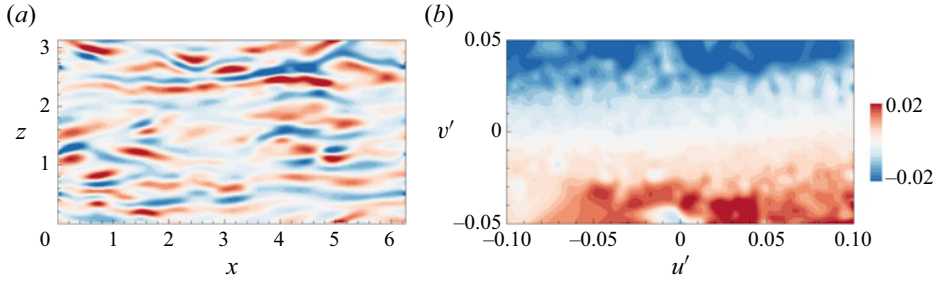

Figure 26. Contours of the instantaneous wall blowing and suction by the RNL-RL model in (*a*) the x–z plane and (*b*) the u'–v' plane at $Re_\tau = 180$. Here u' and v' of (*b*) are from $y^+ = 10$. The wall blowing and suction velocities corresponding to the unsampled u' and v' are obtained through linear interpolation.

Different with the present work, Sonoda *et al.* (2023), Guastoni *et al.* (2023) applied RL to determine the optimal wall blowing and suction with the input of streamwise and normal velocity fluctuations on the detection plane at $y^+ = 15$. Moreover, they used a deep neural network to represent the RL agent. It can be viewed as a point-to-point style, as dictated in (1) of Guastoni *et al.* (2023) and (3.4) and (3.5) of Sonoda *et al.* (2023). The wall blowing and suction at one grid point is only dependent on the streamwise and normal velocities at the same position on the detection plane. On the other hand, since CNN is used as the RL agent in the present study, the wall blowing and suction at a grid point is determined by the wall shear stresses within a certain range around it. So, their control strategy indicates an abrupt switch between strong wall blowing and suction for downwelling of high-speed fluids and upwelling of low-speed fluids. Also, due to the dependence on the streamwise velocity fluctuation on the detection plane, the control strategy of Guastoni *et al.* (2023) shows an inclination angle of the boundary between wall blowing and suction. But our RNL-RL model is almost independent of the streamwise velocity fluctuation, similar with that of opposition control, as shown in figure 26(*b*). The wall blowing and suction explored from our RNL-RL model extends longitudinally in the streamwise direction and alternatively changes along the spanwise direction reflecting instantaneous near-wall streaky structures (figure 26*a*), whereas the wall actuations from their model are uniform in the spanwise direction and the streamwise wavelength is equal to the streamwise domain size. Besides the differences from the input data and the RL architecture, different hyperparameters used for training will also lead to different local optimum solutions (Lee *et al.* 2023).

Furthermore, we also carry out RNL-RL training based on the input of $\partial u/\partial y|_w$; but it does not produce effective drag reduction results, even though the training process is convergent and appears to have drag reduction effects in the RNL field. When applying the trained model to control the DNS flow, the output wall blowing and suction do not produce effective drag reduction. It may be due to the different flow fields in the streamwise direction between the RNL model and DNS for training based on $\partial u/\partial y|_w$. For the SL of CNN discussed in the above sections, even though there are also losses of the information in the streamwise direction, the output of the RNL-SL model can still give acceptable prediction with the guidance of label data. But for the RNL-RL model, the adjustment of the action is completely dependent on the value function adopted by the RL agent based on its observation of the flow environment. In this case, the restriction in the streamwise direction makes the RNL-RL model trained by RNL data not applicable in control of the DNS flow field. This needs to be further investigated in the future. As for a

preliminary attempt of combining the RNL model with RL, successful application based on the spanwise wall shear stress to the turbulent channel flow at up to $Re_\tau = 950$ provides us an enlightening insight that a physical reduced-order model can overcome the difficulty of high computational cost in the RL training and improve the feasibility of applying a machine learning control method to practical situations.

5. Conclusions

In the present study an efficient flow control method, which combines the RNL model with machine learning technology, was developed for drag reduction in turbulent channel flow, aiming at reducing the training cost of the machine learning control. By eliminating the streamwise varying perturbation–perturbation nonlinearity, the RNL model is used as a reduced-order model to carry out simulation of the wall turbulence economically. The machine learning control model is designed to predict effective wall blowing and suction to weaken the streamwise vortices.

Firstly, the coupled RNL-SL control model is trained by RNL data to predict the normal velocities at a detection plane at $y^+ = 10$ as wall blowing and suction based on streamwise or spanwise wall shear stress. The architecture of the RNL-SL model is constructed in a manner similar to our previous investigation (Han & Huang 2020), in which a linear single-layer CNN is employed for prediction using the spanwise wall shear stress as input, while a CNN with multiple nonlinear convolutional layers is utilized with the streamwise wall shear stress. Although the flow field of RNL simulation shows some differences with those of DNS, the well-trained RNL-SL model exhibits remarkable resemblance to the CNN model trained using DNS data (Han & Huang 2020) and the analytical solution of the suboptimal control (Lee *et al.* 1998). It indicates that the RNL model captures the fundamental self-sustaining mechanism in turbulent channel flow especially in the near-wall region. The RNL-SL model is tested in a DNS flow field. Based on the spanwise wall shear stress, the correlation coefficients between the predicted normal velocities and those at the detection plane are 0.85, 0.80 and 0.81, which are slightly lower than those obtained in the test RNL flow field, 0.90, 0.89 and 0.90 at $Re_\tau = 100, 180, 950$, respectively. The prediction performance based on the streamwise wall shear stress in the DNS flow field decreases to about one half of that in RNL flow field. It is because the streamwise information of the flow field has more influence on the training process when using the streamwise wall shear stress as input. However, it is restricted in the RNL simulation resulting in larger differences between the training data from the RNL model and the test one from DNS. The correlation coefficients in DNS based on the streamwise wall shear stress are 0.60, 0.40 and 0.36 at $Re_\tau = 100, 180, 950$, respectively. This also shows the linear relationship between the predicted value and the label data, and it is still applicable for flow control. Active control of the DNS flow field is carried out using the wall blowing and suction determined by the RNL-SL model. Drag reduction rates are over 16 % using the RNL-SL model with the spanwise wall shear stresses at the Reynolds number of up to $Re_\tau = 950$, and 12 % using the streamwise wall shear stress. These results indicate that the RNL model is effective for predicting the optimal wall blowing and suction to reduce the drag in the turbulent channel flow. It enables significant savings in computational cost, which can be used as a physical reduced-order model for accelerating the training of the machine learning control model.

Furthermore, we also tested a control strategy based on the wall quantities only, without the need of the label data on the detection plane, which is hard to acquire in real practice. A semi-supervised machine learning method of RL can optimize the control strategy by analysing the reward of control without the label data. It is well known that RL relies

much on the simulation speed of the flow field since it is an online learning process, where the controlling and training processes are conducted synchronously. In the present study we attempted to explore the possibility of combining the RNL model with RL to determine the optimal wall blowing and suction based on the spanwise wall shear stress. With the help of the RNL model, the RNL-RL model discovers the effective control strategy, which achieves similar drag reduction rates as reported in the previous studies, but with significantly reduced learning cost. Compared with the results of Lee *et al.* (2023), the training cost of our RNL-RL model is decreased by over thirty times at $Re_\tau = 950$ since much fewer grids are used in the RNL model. The control strategy discovered by the RNL-RL model was also investigated. By analysing the influence of wall blowing and suction on the streamwise vortices, it was found that with the input of spanwise wall shear stress, RNL-RL applies blowing and suction to suppress the streamwise vortices in a similar way with the opposition control. In addition, we also carried out the training of the RNL-RL model based on the streamwise wall shear, but the lack of flow information in the streamwise direction of the RNL model makes it difficult for RNL-RL to learn an effective and convergent control strategy. So it remains to be explored in the future. The present results provide a perspective that it is feasible to extend the application of the machine learning control method to the flow field at higher Reynolds numbers by coupling a physical reduced-order model to keep the learning cost within an acceptable range. The RNL model has been proven to be a good choice, especially for drag reduction in wall turbulence.

Funding. This work was supported by the National Natural Science Foundation of China under grant nos 12272206, 92252204 and 12388101.

Declaration of interest. The authors report no conflict of interest.

Author ORCIDs.
Wei-Xi Huang https://orcid.org/0000-0003-4149-3369;
Chun-Xiao Xu https://orcid.org/0000-0001-5292-8052.

Appendix A. Open source code

The source code of this project is released as open source on the GitHub of the author: https://github.com/Bingzheng-Han/RNL-ML-control.

Appendix B. Comparison between RNL and DNS flow fields

Figure 27 shows the instantaneous wall-normal velocity from RNL flow fields compared with that from DNS flow. Similar with the results of the streamwise velocity, The normal velocity at $y^+ = 10$ also show a visible restriction of the streamwise wavenumbers and present an elongated streak in the streamwise direction. In the spanwise direction, because of the usage of the same grid resolution, alternating positive and negative velocity fluctuations in RNL fields are similar to DNS. These phenomena are consistent for both $Re_\tau = 180$ and $Re_\tau = 950$.

From the instantaneous streamwise vorticity in the y–z plane shown in figure 28, the overall distribution of ω_x in the RNL model is very similar to that in DNS, especially in the near-wall region where the amplitudes of ω_x are the largest. It indicates that the restriction of the streamwise wavenumbers does not affect the RNL model's prediction of streamwise vortices. The r.m.s. fluctuations of the streamwise, wall-normal and spanwise vorticities at $Re_\tau = 180$ and $Re_\tau = 950$ are shown in figure 29. The results from RNL

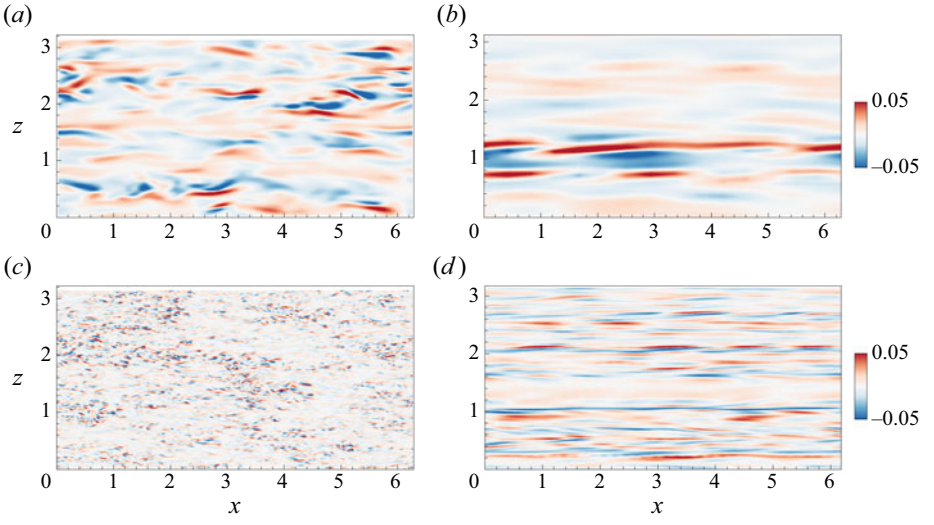

Figure 27. Comparison of the instantaneous normal velocity between (*a*,*c*) DNS and (*b*,*d*) the RNL model at $y^+ = 10$: (*a*,*b*) $Re_\tau = 180$ and (*c*,*d*) $Re_\tau = 950$.

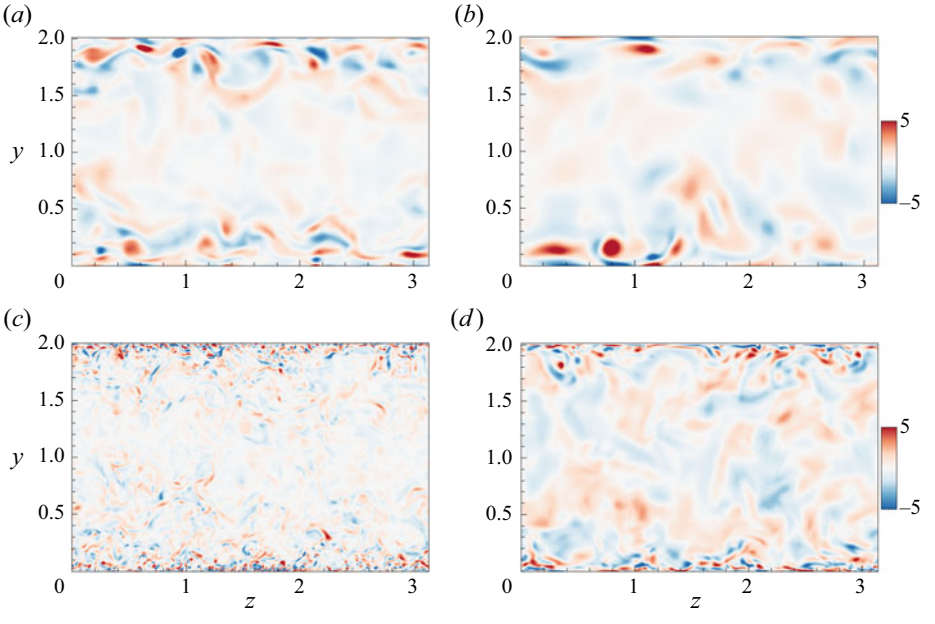

Figure 28. Comparison of the instantaneous streamwise vorticity between (*a*,*c*) DNS and (*b*,*d*) the RNL model: (*a*,*b*) $Re_\tau = 180$ and (*c*,*d*) $Re_\tau = 950$.

fields are all similar with those from DNS, but there are several differences in both the inner- and buffer-layer regions. Even though the magnitude of the r.m.s. of the streamwise vorticity is under-predicted because the small scales that dominate the near wall and buffer-layer vorticity are under-resolved in the RNL model, the locations of the maximum and minimum values in the near-wall region are consistent with DNS, which has also been reported by Gayme & Minnick (2019). The position of the maximum value

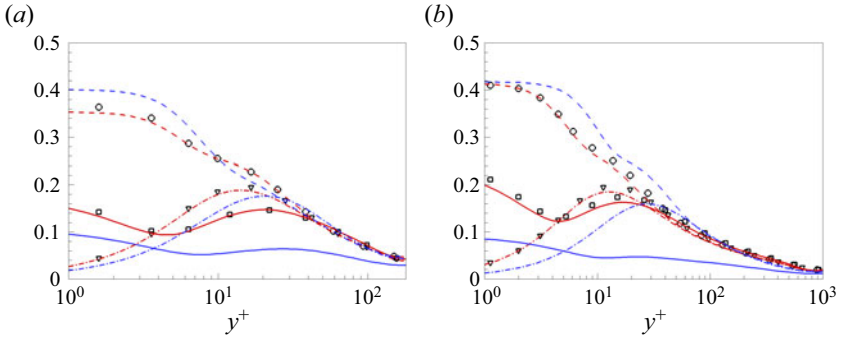

Figure 29. Comparison of the r.m.s. fluctuations of the streamwise (—), normal (– –) and spanwise (- · -) vorticities normalized by the wall shear stress: (*a*) $Re_\tau = 180$ and (*b*) $Re_\tau = 950$. Symbols of □, ∇, ○ representing streamwise, normal and spanwise vorticities from Kim *et al.* (1987). Red lines are the results from DNS and blue lines are from the RNL model.

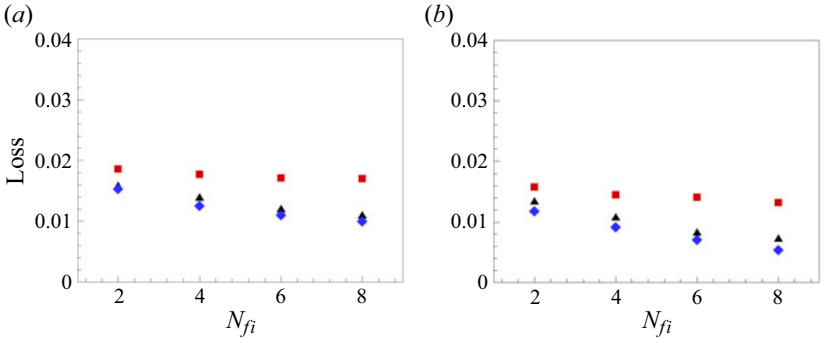

Figure 30. Variations of the loss with the number of the filter kernels (N_{fi}) and convolutional layers (■ for 2, ▲ for 4 and ♦ for 6) used in the CNN architecture based on the streamwise wall shear stress at $Re_\tau = 180$: (*a*) the filter kernel size is 3 × 3, (*b*) the filter kernel size is 5 × 5.

can be considered to be the position of the centre of the streamwise vortices, and the distance between the minimum and the maximum locations represents the mean radius of streamwise vortices (Kim, Moin & Moser 1987). Accordingly, the RNL model is able to predict the streamwise vortices near the wall.

Appendix C. Parametric study on CNN

As shown in table 2, there are three main hyperparameters related to CNN, i.e. number of the convolutional layers, size of the filter kernel and number of filter kernels in each convolutional layer. Taking the RNL-SL model based on the streamwise wall shear stress at $Re_\tau = 180$ as an example, it is seen in figure 30 that increasing the number of convolutional layers and the filter kernels used in each layer reduces the loss between the output of CNN and the label data. However, it is observed that regardless of the number of convolutional layers employed, errors with 8 filter kernels per layer remain roughly the same as those with 6 kernels per layer. Also, increasing the number of convolutional layers from 4 to 6 does not decrease the loss substantially. Furthermore, the training losses obtained with 5 × 5 filter kernels are always smaller than those obtained with 3 × 3 filter kernels. Therefore, a CNN model with 4 convolutional layers, each using six 5 × 5 filter kernels, is employed

in predicting the optimal wall blowing and suction based on the streamwise wall shear stress at $Re_\tau = 180$, as listed in table 2.

Appendix D. Algorithm of DDPG

As introduced in § 2.3, DDPG consists of two networks: the actor network (μ_{θ^μ}) and the critic network (Q_{θ^Q}). Here θ^μ is optimized by maximizing the expected total reward Q_{θ^Q}. To update θ^Q, it needs to obtain the Bellman equation by making use of the recursive relationship

$$Q_{\theta^Q}(s_t, a_t) = \mathbb{E}[r(s_t, a_t) + \gamma Q_{\theta^Q}(s_{t+1}, a_{t+1})], \tag{D1}$$

where $a_{t+1} = \mu_{\theta^\mu}(s_{t+1})$. Since (D1) is derived without any estimation, $Q_{\theta^Q}(s_t, a_t)$ from (D1) is thought to be the target value and the evaluation value by the critic work from (2.7) should be as close as possible to it. Thus, θ^Q is optimized to minimize the loss:

$$L(\theta^Q) = \mathbb{E}[(r(s_t, a_t) + \gamma Q_{\theta^Q}(s_{t+1}, a_{t+1}) - Q_{\theta^Q}(s_t, a_t))^2]. \tag{D2}$$

Since the updated network Q_{θ^Q} is also used in calculating the target value (D1), the updating is prone to divergence (Lillicrap *et al.* 2015). It can be solved by using another network $Q_{\theta^{Q'}}$, which shares the same architecture as the critic network but is updated asynchronously with it to calculate the target value in (D1) (Mnih *et al.* 2013). When updating $\theta^{Q'}$, the soft weight update method proved by Lillicrap *et al.* (2015) is applied, i.e. $\theta^{Q'} = \tau\theta^Q + (1-\tau)\theta^{Q'}$, to increase the stability of training, where $\tau = 0.01$ in the present study. A similar operation is also applied to utilize a target actor network $\mu_{\theta^{\mu'}}$ for calculating the next action $a_{t+1} = \mu_{\theta^{\mu'}}(s_{t+1})$ in (D1).

References

Alizard, F. & Biau, D. 2019 Restricted nonlinear model for high-and low-drag events in plane channel flow. *J. Fluid Mech.* **864**, 221–243.

Bewley, T.R. & Protas, B. 2004 Skin friction and pressure: the 'footprints' of turbulence. *Phys. D: Nonlinear Phenom.* **196** (1–2), 28–44.

Breiman, L. 2001 Random forests. *Mach. Learn.* **45**, 5–32.

Bretheim, J.U., Meneveau, C. & Gayme, D.F. 2015 Standard logarithmic mean velocity distribution in a band-limited restricted nonlinear model of turbulent flow in a half-channel. *Phys. Fluids* **27** (1), 011702.

Bretheim, J.U., Meneveau, C. & Gayme, D.F. 2018 A restricted nonlinear large eddy simulation model for high Reynolds number flows. *J. Turbul.* **19** (2), 141–166.

Chang, Y., Collis, S.S. & Ramakrishnan, S. 2002 Viscous effects in control of near-wall turbulence. *Phys. Fluids* **14** (11), 4069–4080.

Choi, H., Moin, P. & Kim, J. 1994 Active turbulence control for drag reduction in wall-bounded flows. *J. Fluid Mech.* **262**, 75–110.

Chung, Y.M. & Talha, T. 2011 Effectiveness of active flow control for turbulent skin friction drag reduction. *Phys. Fluids* **23** (2), 025102.

Constantinou, N.C., Lozano-Durán, A., Nikolaidis, M.-A., Farrell, B.F., Ioannou, P.J. & Jiménez, J. 2014 Turbulence in the highly restricted dynamics of a closure at second order: comparison with DNS. *J. Phys.: Conf. Ser.* **506**, 012004.

Deng, B.-Q., Huang, W.-X. & Xu, C.-X. 2016 Origin of effectiveness degradation in active drag reduction control of turbulent channel flow at $re\tau = 1000$. *J. Turbul.* **17** (8), 758–786.

Deng, B.-Q. & Xu, C.-X. 2012 Influence of active control on STG-based generation of streamwise vortices in near-wall turbulence. *J. Fluid Mech.* **710**, 234–259.

Fan, D., Yang, L., Wang, Z., Triantafyllou, M.S. & Karniadakis, G.E. 2020*a* Reinforcement learning for bluff body active flow control in experiments and simulations. *Proc. Natl Acad. Sci.* **117** (42), 26091–26098.

Fan, D., Yang, L., Wang, Z., Triantafyllou, M.S. & Karniadakis, G.E. 2020*b* Reinforcement learning for bluff body active flow control in experiments and simulations. *Proc. Natl Acad. Sci.* **117** (42), 26091–26098.

FARRELL, B.F. & IOANNOU, P.J. 2012 Dynamics of streamwise rolls and streaks in turbulent wall-bounded shear flow. *J. Fluid Mech.* **708**, 149–196.

FARRELL, B.F., IOANNOU, P.J., JIMÉNEZ, J., CONSTANTINOU, N.C., LOZANO-DURÁN, A. & NIKOLAIDIS, M.-A. 2016 A statistical state dynamics-based study of the structure and mechanism of large-scale motions in plane Poiseuille flow. *J. Fluid Mech.* **809**, 290–315.

FUKAGATA, K. & KASAGI, N. 2004 Suboptimal control for drag reduction via suppression of near-wall Reynolds shear stress. *Intl J. Heat Fluid Flow* **25** (3), 341–350.

FUKAMI, K., NABAE, Y., KAWAI, K. & FUKAGATA, K. 2019 Synthetic turbulent inflow generator using machine learning. *Phys. Rev. Fluids* **4** (6), 064603.

GAYME, D.F. & MINNICK, B.A. 2019 Coherent structure-based approach to modeling wall turbulence. *Phys. Rev. Fluids* **4** (11), 110505.

GE, M.-W., XU, C.-X. & CUI, G.-X. 2011 Detection of near-wall streamwise vortices by measurable information at wall. *J. Phys.: Conf. Ser.* **318**, 022040.

GUASTONI, L., RABAULT, J., SCHLATTER, P., AZIZPOUR, H. & VINUESA, R. 2023 Deep reinforcement learning for turbulent drag reduction in channel flows. *Eur. Phys. J.* E **46** (4), 27.

GUO, X., LI, W. & IORIO, F. 2016 Convolutional neural networks for steady flow approximation. In *Proceedings of the 22nd ACM SIGKDD International Conference on Knowledge Discovery and Data Mining*, Association for Computing Machinery, New York, NY, United States, pp. 481–490.

HAMILTON, J.M., KIM, J. & WALEFFE, F. 1995 Regeneration mechanisms of near-wall turbulence structures. *J. Fluid Mech.* **287**, 317–348.

HAMMOND, E.P., BEWLEY, T.R. & MOIN, P. 1998 Observed mechanisms for turbulence attenuation and enhancement in opposition-controlled wall-bounded flows. *Phys. Fluids* **10** (9), 2421–2423.

HAN, B.-Z. & HUANG, W.-X. 2020 Active control for drag reduction of turbulent channel flow based on convolutional neural networks. *Phys. Fluids* **32** (9), 095108.

HAN, B.-Z., HUANG, W.-X. & XU, C.-X. 2022 Deep reinforcement learning for active control of flow over a circular cylinder with rotational oscillations. *Intl J. Heat Fluid Flow* **96**, 109008.

JIMÉNEZ, J. & MOIN, P. 1991 The minimal flow unit in near-wall turbulence. *J. Fluid Mech.* **225**, 213–240.

KASAGI, N., SUZUKI, Y. & FUKAGATA, K. 2009 Microelectromechanical systems-based feedback control of turbulence for skin friction reduction. *Annu. Rev. Fluid Mech.* **41**, 231–251.

KIM, E. & CHOI, H. 2017 Linear proportional–integral control for skin-friction reduction in a turbulent channel flow. *J. Fluid Mech.* **814**, 430–451.

KIM, J. 2011 Physics and control of wall turbulence for drag reduction. *Phil. Trans. R. Soc.* A*: Math. Phys. Engng Sci.* **369** (1940), 1396–1411.

KIM, J. & LEE, C. 2020 Prediction of turbulent heat transfer using convolutional neural networks. *J. Fluid Mech.* **882**, A18.

KIM, J., MOIN, P. & MOSER, R. 1987 Turbulence statistics in fully developed channel flow at low Reynolds number. *J. Fluid Mech.* **177**, 133–166.

KIM, K., BAEK, S.-J. & SUNG, H.J. 2002 An implicit velocity decoupling procedure for the incompressible Navier–Stokes equations. *Intl J. Numer. Meth. Fluids* **38** (2), 125–138.

KOUMOUTSAKOS, P. 1999 Vorticity flux control for a turbulent channel flow. *Phys. Fluids* **11** (2), 248–250.

KRAVCHENKO, A.G., CHOI, H. & MOIN, P. 1993 On the relation of near-wall streamwise vortices to wall skin friction in turbulent boundary layers. *Phys. Fluids* A*: Fluid Dyn.* **5** (12), 3307–3309.

LEE, C., KIM, J., BABCOCK, D. & GOODMAN, R. 1997 Application of neural networks to turbulence control for drag reduction. *Phys. Fluids* **9** (6), 1740–1747.

LEE, C., KIM, J. & CHOI, H. 1998 Suboptimal control of turbulent channel flow for drag reduction. *J. Fluid Mech.* **358**, 245–258.

LEE, K.H., CORTELEZZI, L., KIM, J. & SPEYER, J. 2001 Application of reduced-order controller to turbulent flows for drag reduction. *Phys. Fluids* **13** (5), 1321–1330.

LEE, T., KIM, J. & LEE, C. 2023 Turbulence control for drag reduction through deep reinforcement learning. *Phys. Rev. Fluids* **8** (2), 024604.

LILLICRAP, T.P., HUNT, J.J., PRITZEL, A., HEESS, N., EREZ, T., TASSA, Y., SILVER, D. & WIERSTRA, D. 2015 Continuous control with deep reinforcement learning. Preprint, arXiv:1509.02971.

LORANG, L.V., PODVIN, B. & LE QUÉRÉ, P. 2008 Application of compact neural network for drag reduction in a turbulent channel flow at low Reynolds numbers. *Phys. Fluids* **20** (4), 045104.

MNIH, V., KAVUKCUOGLU, K., SILVER, D., GRAVES, A., ANTONOGLOU, I., WIERSTRA, D. & RIEDMILLER, M. 2013 Playing atari with deep reinforcement learning. Preprint, arXiv:1312.5602.

MORIMOTO, K., IWAMOTO, K., SUZUKI, Y. & KASAGI, N. 2002 Genetic algorithm-based optimization of feedback control scheme for wall turbulence. In *Proceedings of the 3rd Symposium on Smart Control of Turbulence*, pp. 107–113.

NAIR, V. & HINTON, G.E. 2010 Rectified linear units improve restricted Boltzmann machines. In *Proceedings of the 27th International Conference on Machine Learning (ICML-10)*, pp. 807–814.

PARIS, R., BENEDDINE, S. & DANDOIS, J. 2021 Robust flow control and optimal sensor placement using deep reinforcement learning. *J. Fluid Mech.* **913**, A25.

PARK, J. & CHOI, H. 2020 Machine-learning-based feedback control for drag reduction in a turbulent channel flow. *J. Fluid Mech.* **904**, A24.

RABAULT, J., KUCHTA, M., JENSEN, A., RÉGLADE, U. & CERARDI, N. 2019 Artificial neural networks trained through deep reinforcement learning discover control strategies for active flow control. *J. Fluid Mech.* **865**, 281–302.

SCHOPPA, W. & HUSSAIN, F. 2002 Coherent structure generation in near-wall turbulence. *J. Fluid Mech.* **453**, 57–108.

SMITH, T.R., MOEHLIS, J. & HOLMES, P. 2005 Low-dimensional modelling of turbulence using the proper orthogonal decomposition: a tutorial. *Nonlinear Dyn.* **41**, 275–307.

SONODA, T., LIU, Z., ITOH, T. & HASEGAWA, Y. 2023 Reinforcement learning of control strategies for reducing skin friction drag in a fully developed turbulent channel flow. *J. Fluid Mech.* **960**, A30.

TANG, H., RABAULT, J., KUHNLE, A., WANG, Y. & WANG, T. 2020 Robust active flow control over a range of Reynolds numbers using an artificial neural network trained through deep reinforcement learning. *Phys. Fluids* **32** (5), 053605.

THOMAS, V.L., FARRELL, B.F., IOANNOU, P.J. & GAYME, D.F. 2015 A minimal model of self-sustaining turbulence. *Phys. Fluids* **27** (10), 105104.

THOMAS, V.L., LIEU, B.K., JOVANOVIĆ, M.R., FARRELL, B.F., IOANNOU, P.J. & GAYME, D.F. 2014 Self-sustaining turbulence in a restricted nonlinear model of plane Couette flow. *Phys. Fluids* **26** (10), 105112.

TIBSHIRANI, R. 1996 Regression shrinkage and selection via the lasso. *J. R. Stat. Soc. Ser.* B*: Stat. Methodol.* **58** (1), 267–288.